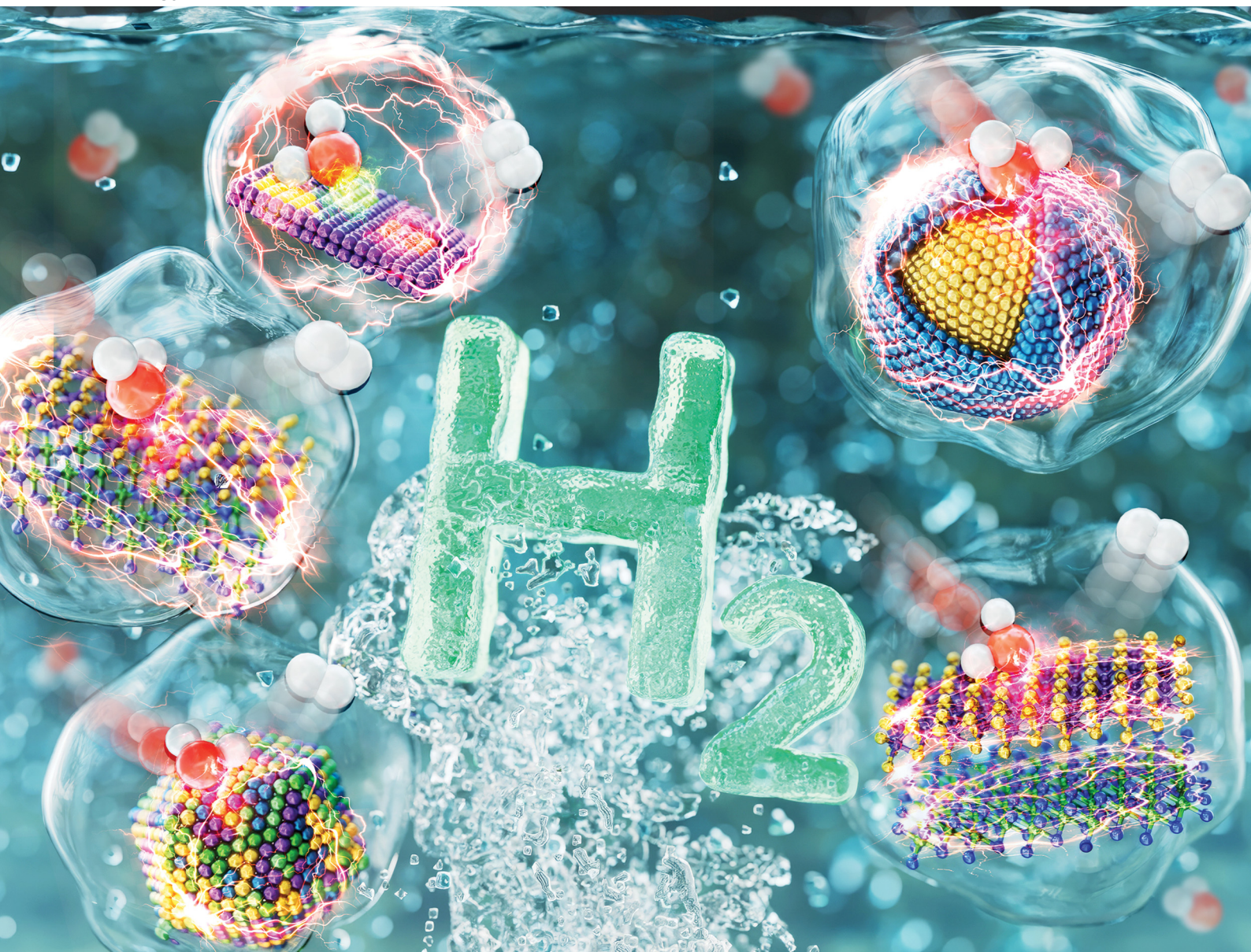


# Energy Advances

Volume 4  
Number 6  
June 2025  
Pages 711–812

[rsc.li/energy-advances](https://rsc.li/energy-advances)



ISSN 2753-1457

Cite this: *Energy Adv.*, 2025,  
4, 716

# Interface engineering strategies for enhanced electrocatalytic hydrogen evolution reaction

Manjinder Singh, <sup>ab</sup> Dasu Ram Paudel, <sup>c</sup> Hayoung Kim, <sup>bd</sup>  
Tae Hyeong Kim, <sup>bd</sup> Jaejun Park <sup>bd</sup> and Seunghyun Lee <sup>\*abd</sup>

Producing hydrogen as a clean and sustainable fuel source requires an in-depth understanding of the hydrogen evolution reaction (HER), which plays a pivotal role in energy conversion processes. Recently, significant interest has been expressed in utilizing transition-metal-based nanomaterials as potential electrocatalysts for the HER owing to their exceptional electrical properties, versatile surface chemistry, and robust catalytic activity. These nanomaterials could enhance the efficiency of hydrogen production when carefully engineered at the interface level. Interface engineering has emerged as a critical strategy for optimizing the surface and interfacial characteristics of nanomaterials, thereby improving their catalytic efficiency. This review provides a comprehensive and detailed overview of the various aspects of interface engineering in the context of transition metal-based nanomaterial electrocatalysts specifically tailored for the HER. The fundamental characteristics of interfaces are described and their role in influencing catalytic performance is emphasized. Key factors, such as atomic arrangements, grain boundaries, and surface imperfections, are explored to better understand their impact on catalytic activity. A range of innovative interface engineering techniques have been used to enhance the catalytic performance of nanomaterial-based electrocatalysts. The techniques include the creation of heterostructures that allow for improved charge separation and enhanced catalytic sites, development of core-shell architectures that can protect active sites while optimizing their accessibility, and manipulation of phase transitions to achieve desirable catalytic properties. Additionally, alloying techniques and the incorporation of single-atom catalysts, which are methods used to fine-tune the electronic and structural attributes of nanomaterials, are discussed. Furthermore, this review highlights recent advancements and prospective pathways in the electrocatalytic processes of the HER and features emerging technologies/methodologies. The review concludes with a thorough discussion of the limitations of nanomaterials, particularly those related to interface stability, scalability, and commercialization of efficient HER electrocatalysts. By providing a detailed examination of the latest innovations and challenges in interface engineering, this paper offers valuable perspectives and guidance for future research and real-world applications aimed at advancing the development of highly efficient electrocatalysts for sustainable hydrogen production.

Received 26th January 2025,  
Accepted 29th March 2025

DOI: 10.1039/d5ya00022j

rsc.li/energy-advances

## 1. Introduction

Worldwide, increasing population and economic growth are driving the global energy demand. Currently, this demand is primarily met by non-renewable fossil fuels such as oil, coal, and natural gas, which are finite resources and will deplete

gradually over the coming decades.<sup>1</sup> The use of fossil fuels contributes to environmental deterioration that jeopardizes human life by causing climate change and greenhouse emissions, which frequently result in expensive management expenses.<sup>2–4</sup> Additionally, energy limitations are beginning to constrain economic growth due to environmental pollution and energy depletion. The Sustainable Development Goal (SDG) 7, a global energy goal, has three main objectives: ensuring universal, affordable, and reliable access to modern energy services; substantially increasing the share of renewable energy in the global energy mix; and tripling the rate at which energy efficiency is improving worldwide.<sup>5</sup> Recently, more research has focused on how the various targets of SDG 7 could help achieve other SDGs.

<sup>a</sup> Department of Chemical and Molecular Engineering, Hanyang University ERICA, Ansan, 15588, Republic of Korea. E-mail: leeshyun@hanyang.ac.kr

<sup>b</sup> Center for Bionano Intelligence Education and Research, Hanyang University ERICA, Ansan, 15588, Republic of Korea

<sup>c</sup> Department of Chemistry, Tri-Chandra Multiple Campus, Tribhuvan University, Kathmandu, 44613, Nepal

<sup>d</sup> Department of Applied Chemistry, Hanyang University ERICA, Ansan, 15588, Republic of Korea



A worldwide energy shift is urgently needed to accomplish the goal of ensuring the average increase in the global surface temperature remains below 2 °C. A shift from fossil fuels to low-carbon alternatives is imperative because energy-related carbon dioxide (CO<sub>2</sub>) emissions account for two-thirds of greenhouse gas (GHG) emissions worldwide.<sup>6</sup> Switching from fossil fuels to affordable, eco-friendly materials is essential to meet the increasing need for energy for sustainable and economic development. Because the existing energy models do not yet adequately satisfy the net-zero emission target of the energy sector, an intermediate goal is required in addition to any long-term net-zero objective. A key solution to the energy shortage and environmental problems is the rapid development of green power sources such as high-performance fuel cells and metal-air batteries.<sup>7,8</sup> Hydrogen is renewable, emits zero emissions, and is environmentally benign, making it a viable alternative to fossil fuels.<sup>9,10</sup>

Moreover, hydrogen has a higher energy content than that of natural gasoline and can be obtained from diverse sources; moreover, hydrogen has added advantages of nontoxicity and ease of storage through chemical or physiochemical means. The hydrogen energy vector offers an alternative to battery

storage for electricity because its conversion back into electricity through fuel cells enables independent scaling of power and energy. In contrast to oil and natural gas, hydrogen serves as an energy carrier rather than a direct energy source for storage and transportation purposes.<sup>11</sup> The benefits of hydrogen are widespread in many chemical industries, metallurgy, agriculture, and aerospace, among others, and common industrial products such as iron, aluminum, and ammonia could be produced at lower costs.<sup>12</sup> Because of its high energy density and ability to produce energy with no emissions, green hydrogen has become a promising clean energy carrier. Green energy sources are increasingly popular for hydrogen production with the development of renewable energy landscapes. Research into hydrogen production and fuel cells, vital for both its production and use, is crucial as hydrogen is considered the best alternative to fossil fuels and is the backbone of the hydrogen energy economy.<sup>13</sup> Accordingly, electrochemical energy conversion technologies and their electrode reactions are highly relevant, green topics worldwide.

Water-splitting technologies are extensively used for hydrogen production in energy conversion processes and leverage the stability of water.<sup>14</sup> This technique efficiently utilizes large



**Manjinder Singh**

*research focuses on the synthesis of transition metal dichalcogenides for energy conversion applications.*

*Manjinder Singh received his PhD in Engineering from Jeonbuk National University, South Korea, in 2023 under the supervision of Prof. Joong Hee Lee. He obtained a Masters of Technology in Nanotechnology from Shri Guru Granth Sahib World University, India, in 2017. As a post-doctoral researcher, Manjinder joined Prof. Seunghyun Lee's lab at Hanyang University, South Korea in March 2023. His*



**Dasu Ram Paudel**

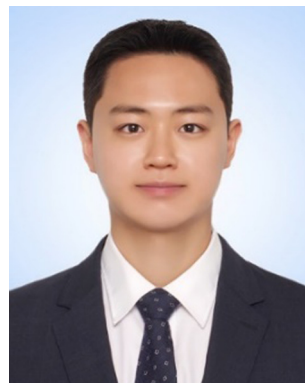
*fabrication of nanomaterials with prospective applications in energy storage and conversion.*

*Dasu Ram Paudel is an Assistant Professor of Chemistry at Tribhuvan University, Kathmandu, Nepal. He received his PhD degree from the Department of Nano Convergence Engineering, Jeonbuk National University, South Korea, under the supervision of Prof. Joong Hee Lee. Dasu obtained his MSc in inorganic chemistry from Tribhuvan University, Nepal. His research interest centers on material chemistry for the design and*



**Hayoung Kim**

*Hayoung Kim is a PhD student in Professor Seunghyun Lee's group at Hanyang University. She received her bachelor's degree from Hanyang University, South Korea in 2023. Her research interests focus on metal oxide hybrid nanostructures for energy conversion application and density functional theory calculation for energy conversion.*



**Tae Hyeong Kim**

*Tae Hyeong Kim received his bachelor's and master's degrees in Nanochemistry from Gachon University, South Korea, in 2019 and 2021, respectively. He is currently a PhD student in Prof. Seunghyun Lee's group at Hanyang University, South Korea. Tae's research focuses on the fabrication of nanocarbons and their composites with metal oxide nanoparticles for energy applications.*



quantities of water to generate high-quality green hydrogen at a low cost, with no emission of CO<sub>2</sub> or other pollutants, and without requiring high temperatures. The water-splitting process involves sluggish electrochemical reactions, namely the oxygen evolution reaction (OER) and hydrogen evolution reaction (HER).<sup>15</sup> Green hydrogen obtained *via* the use of renewable energy by the water-splitting process could play a key role as a clean energy vector. Electrocatalysts are vital components of electrochemical processes because they operate on electrode surfaces, facilitating the necessary reactions. The water-splitting thermodynamically demanding reaction requires a high thermodynamic Gibb's free energy ( $\Delta G \approx 237.2 \text{ kJ mol}^{-1}$ ) and the corresponding standard cell potential of 1.23 V vs. RHE (reversible hydrogen electrode).<sup>16</sup> To overcome the kinetic barriers, the additional energies required are the high overpotentials and low faradaic efficiency. Hence, electrocatalysts are necessary to lower the overpotential of the processes involved in electrocatalysis; these processes involve oxidation and reduction reactions through the direct transfer of electrons.<sup>17</sup> An effective electrocatalyst can minimize the overpotential needed to drive a particular electrochemical process. Therefore, the development of efficient and durable bifunctional non-precious-metal electrocatalysts for water-splitting is an urgent requirement in the hydrogen production industry.

Transition metals (TMs) (such as Fe, Rh, Pd, Ir, Pt, Mo, W, Re, Co, Ni, *etc.*) and their derived nanomaterials, namely, alloys and compounds are reportedly effective electrocatalysts for the HER.<sup>18</sup> From a chemical perspective, the electrocatalytic reactions during the HER occur at the catalyst surface or interfaces and the surface electrical structure and properties determine their catalytic efficacy. Although TMs and their derived electrocatalysts are advantageous for electrochemical water-splitting

because of their abundant natural reserves, low cost, tunable electronic structure, versatile oxidation state, perfect catalytic performance, adjustable electronic conductivity, long operational stability, and high-valence metal sites.<sup>19</sup> TM oxides (spinel and perovskite), chalcogenides, Janus chalcogenides, carbides, borides, phosphides, nitrides, oxyhydroxides, and alloys are more suited to electrochemical catalytic applications. Park *et al.* reported a composite of Ni and Mo-based nitride nanoparticles (Ni<sub>2</sub>Mo<sub>3</sub>N) grown on nickel foam (NF) and studied its HER activity.<sup>20</sup> The derived Ni<sub>2</sub>Mo<sub>3</sub>N/NF exhibited high activity with low overpotentials (21.3 mV at 10 mA cm<sup>-2</sup>) and excellent stability for the HER, achieving one of the best performances among state-of-the-art TM nitride-based catalysts in alkaline media. Shalom *et al.* derived pure nickel nitride (Ni<sub>3</sub>N) and verified its HER activity with an overpotential of 50 mV at 10 mA cm<sup>-2</sup>.<sup>21</sup> However, the current practical applications of these individual materials are still limited, and advancements in material design, particularly in structural architecture, controlled synthetic strategies, and interfacial assembly, are crucial for research in material science.

This review begins with a comprehensive introduction to the fundamental principles and mechanisms underlying the HER in both alkaline and acidic environments. It explores how these conditions influence the electrochemical processes involved in the HER, highlighting the importance of the interplay of electron transfer processes, adsorption energy, and stabilization of surface intermediates for optimizing the overall efficiency of the HER. Following this, we delve into the essential characteristics of interface engineering as it pertains to catalysts designed for alkaline and acidic HER. Furthermore, this review presents a detailed overview of several innovative strategies used in interface engineering. The concept of phase



Jaejun Park

Jaejun Park received his BS degree from Hanyang University, South Korea in 2022. He is currently a PhD student in Prof. Seunghyun Lee's group at Hanyang University. Jaejun's research focuses on the synthesis of silica-based core-shell nanoparticles as electrochemical catalysts and density functional theory calculation for energy conversion.



Seunghyun Lee

Seunghyun Lee is an Associate Professor in the Department of Chemical and Molecular Engineering at Hanyang University ERICA. He also holds adjunct positions in the Department of Bionano Engineering and the HYU-KITECH Joint Department. Prof. Lee received his BSc in Chemical Engineering and MSc in Chemistry from Hanyang University, Seoul, Korea, and earned his PhD in Chemistry from Rice University. Prof. Lee's research group focuses on the synthesis of nanostructured materials, exploring their structural features, surface modifications, and the physicochemical properties of core-shell nanoparticles and heterogeneous nanostructures. Recently, his group has been focused on the development of multicomponent heterostructures as photocatalytic and electrochemical catalysts for biomass energy conversion and green hydrogen production via water-splitting.



engineering is discussed, with a particular focus on how the manipulation of material phases can enhance catalytic performance. We also discuss interface tuning through alloying techniques, which can significantly improve catalyst functionality. Furthermore, we examine single-atom catalysts, which is a leading approach in which individual metal atoms act as active sites, promoting high-efficiency interface-engineered catalysis. This section presents a comparative analysis of noble-metal-based catalysts, such as platinum and palladium, and non-noble-metal alternatives, including TM carbides, phosphides, nitrides, and chalcogenides. We discuss ways to facilitate efficient hydrogen production by focusing on aspects such as surface activity, stability, and overall efficiency. This review provides a comprehensive overview of the mechanisms that contribute to the promotion of catalytic activity in interface-engineered materials. We summarize the various synthesis methods used to create advanced catalysts and their implications for future research, as well as the challenges and emerging trends in interface engineering. The design principles and emerging strategies discussed in this review are intended to serve as valuable resources for researchers and practitioners in this field. By providing insights into the development of interfacial engineering in the HER, we hope to inspire further innovations in nanosized catalyst design that could lead to an enhanced efficiency of hydrogen production through electrocatalysis.

## 2. Interface engineering

The concept of the “interface” in electrocatalysis refers to the strategic combination and interaction between different materials or phases in electrocatalytic systems. This combination plays a critical role in regulating the electronic structure, facilitating electron transfer, enhancing mass transport, and adjusting the binding energy of reaction intermediates, thereby collectively contributing to the acceleration of electrocatalytic activities.<sup>22,23</sup> The field of interface engineering encompasses complex processes involved in creating heterostructures and heterojunctions, altering the interfacial composition, and adjusting the interface area. However, the formation of interfaces in electrocatalysts can be either controllable or uncontrollable, based on the method of fabrication employed. Controllable techniques, including atomic layer deposition (ALD), electrodeposition, physical vapor deposition (PVD), chemical vapor deposition (CVD), molecular beam epitaxy (MBE), sol-gel synthesis, self-assembly, and nano-templating, facilitate precise adjustments of interface characteristics, encompassing morphology, composition, and electronic structure.<sup>24</sup> These approaches make it possible to develop highly efficient and stable electrocatalysts with customized catalytic performance. Conversely, some methods result in partial control or spontaneous interface development, such as thermal annealing, electrochemical cycling, spontaneous oxidation or reduction, chemical etching, and plasma treatment.<sup>25</sup> These techniques can bring about alterations in the interface

through phase segregation, structural rearrangement, or surface modification, frequently leading to unpredictable or fluctuating catalyst behavior. The selection of a method is influenced by the required degree of control and the specific application needs in electrocatalysis. Several strategies can lead to the introduction of interface engineering in nanomaterials, such as heterostructure and core-shell architectures, phase engineering, alloying, and single-atom catalysts (Fig. 1).<sup>26</sup> The development of heterojunctions and composite structures plays a pivotal role in enhancing the activity of electrocatalysts.

The intrinsic stability and electronic conductivity of catalysts can be significantly improved by combining different materials to create heterostructures. The interaction between different phases within the heterostructure can facilitate self-driven electron transfer, resulting in an enhanced rate of charge transfer that ultimately benefits the catalytic reaction.<sup>32</sup> Furthermore, electron redistribution may occur at the boundary of the heterostructure, contributing to the optimization of the electron transfer process. A substantial interface area is also crucial because it allows for the creation of sufficient channels for charge transfer, thereby promoting improved contact between the electrolyte and catalyst.<sup>33</sup>

### 2.1. Fundamentals and characteristics of interface engineering in the HER

The discipline of interface engineering centers on the deliberate alteration of surface characteristics, electronic properties, and interactions at the interfaces between diverse components in a catalyst system. These interfaces include metal-support interfaces, heterostructures, and composite materials.<sup>34</sup> An essential aspect of interface engineering involves meticulous control over factors such as atomic composition, defect structures, interfacial bonding, and the distribution of active sites. These manipulations are performed to optimize the reaction kinetics and overall efficiency of the catalyst system. The manipulation of interfaces can lead to increases the number of active sites. Interfacial engineering can create new active sites or expose existing ones. For example, connections between different materials can generate sites with unique electronic properties. Structural changes, like lattice strains or defects, can activate inactive sites and improve access to active ones. This makes previously less reactive areas more catalytic, enhancing overall efficiency.<sup>35</sup> For example, in heterostructures such as metal/metal oxide or metal/phosphide interfaces, the presence of an interface has the potential to increase the number of active sites, thereby improving the efficacy of the catalyst in facilitating the HER.<sup>36,37</sup>

Electron transfer can be augmented during the HER process by customizing the electronic properties of the catalyst through interface engineering. Furthermore, adjusting the interfaces between different materials can lead to modifications in the d-band center, consequently lowering the energy barrier for hydrogen adsorption and desorption, thereby lowering the energy barriers for HER.<sup>38</sup> Moreover, in bimetallic or composite catalysts, the interface between two distinct metals or metal-support systems can generate a synergistic effect that beneficial





Fig. 1 Schematic representation of strategies used for interface engineering such as heterostructure architecture. Reprinted with permission.<sup>27</sup> Copyright 2016, The American Association for the Advancement of Science. Core-shell architecture, Reprinted with permission.<sup>28</sup> Copyright 2016, American Chemical Society. Phase engineering, Reprinted with permission.<sup>29</sup> Copyright 2023, American Chemical Society. Alloying, Reprinted with permission.<sup>30</sup> Copyright 2024, American Chemical Society. Single atom catalysts, Reprinted with permission.<sup>31</sup> Copyright 2020, Springer Nature.

the HER activity. This phenomenon arises when individual components facilitate different reaction steps, such as one material adsorbing hydrogen, while the other catalyzes its evolution.<sup>39</sup> Numerous catalysts for the HER, particularly those based on metals, can be degraded when subjected to harsh conditions, such as acidic or alkaline environments. The stability of these catalysts can be enhanced by interface engineering, which involves managing the interfacial strain between two distinct materials. This approach can effectively improve the overall durability of the catalyst and minimize its degradation during extended use.

Additionally, the establishment of interfaces between the catalyst and protective materials, such as oxides or carbides, can provide a shield to prevent the core material from corrosion or leaching while maintaining its catalytic activity.<sup>40</sup> Interfaces also play a crucial role in stabilizing beneficial defects, such as vacancies, which contribute to catalytic activity without compromising the overall structural stability of the material.<sup>41</sup> Optimization of the adsorption energies of hydrogen intermediates, such as protons or H atoms, through interface

engineering, enables the selective participation of desired intermediates in a given reaction.<sup>42</sup> Interfaces present in heterogeneous catalysts can be tailored to promote specific binding modes that lead to efficient hydrogen production while minimizing side reactions.

In composite catalysts, the interfaces can facilitate distinct interactions between reactants, thus promoting selective pathways for the HER. For example, a metal/metal oxide interface can encourage the selective adsorption of a proton ( $H^+$ ) at metal sites, while concurrently maintaining an efficient electron transfer pathway at the oxide, thereby enhancing the overall selectivity of the reaction.<sup>43</sup>

**2.1.1. Mechanisms of the HER at nanomaterial interfaces.** Strong kinetic barriers prevail for complete chemical transformations, numerous electron transfers, and multistage half-reactions. During the process of electrolyzing water, the anode can oxidize water by producing hydrogen peroxide *via* two-electron transfer reactions or oxygen *via* four-electron transfer pathways. Electrocatalysts can facilitate both chemical pathways. Major research efforts have focused on developing a



deeper understanding of the relationship between material properties and catalytic performance, with the aim of creating highly selective, active, and durable catalysts. The HER is a critical electrochemical process that involves the transfer of two electrons to produce hydrogen molecules from protons in solution. This reaction can proceed *via* two primary pathways: the Volmer–Heyrovsky and Volmer–Tafel pathways.<sup>44</sup> The HER process is initiated by the Volmer step and is the same in both acidic and basic environments but diverges in subsequent steps. In acidic electrolytes, represented in Fig. 2a, the process begins when a proton ( $\text{H}^+$ ) approaches an active site ( $*$ ) on the electrode surface and combines with an electron ( $\text{e}^-$ ) to form a hydrogen atom ( $\text{H}^*$ ).<sup>45</sup> This formation of  $\text{H}^*$  is vital as it sets the stage for further reactions. By contrast, under the alkaline conditions illustrated in Fig. 2b, the source of  $\text{H}^+$  is water ( $\text{H}_2\text{O}$ ), which interacts with an  $\text{e}^-$  to yield  $\text{H}^*$  and simultaneously releases a hydroxyl ion ( $\text{OH}^-$ ).<sup>45</sup> The pathway that leads to  $\text{H}_2$  formation depends significantly on the coverage of the  $\text{H}^*$  on the electrode surface, which can affect the reaction kinetics.

When the coverage of  $\text{H}^*$  is high, multiple  $\text{H}^*$  species can easily bond to produce  $\text{H}_2$  molecules, which primarily follow the Tafel reaction mechanism. This scenario typically signifies

a high reaction rate and corresponds to a situation in which sufficient  $\text{H}^*$  atoms are present on the surface to facilitate the rapid formation of  $\text{H}_2$ . Conversely, when the  $\text{H}^*$  coverage is low, the reaction pathway shifts to the Heyrovsky mechanism. In this case, an  $\text{H}_2$  molecule is formed by combining a single  $\text{H}^*$  atom, an additional ( $\text{H}^+$ ), and an electron in acidic solutions. Alternatively,  $\text{H}_2$  can be generated under alkaline conditions by interaction with an  $\text{H}^*$  atom, a  $\text{H}_2\text{O}$ , and an electron. This dependence on the relative abundance of  $\text{H}^*$  highlights the nuanced balance between the two pathways and their influence on the overall hydrogen production rate during the HER.

The adsorption of  $\text{H}^*$  on the surface of the electrode material is a fundamental step because its interaction with the electrode surface can significantly impact the overall efficiency of the reaction. A pivotal parameter that influences the kinetics of the HER are the hydrogen adsorption energy, represented as  $\Delta E_{\text{H}}$ , and the hydrogen adsorption free energy ( $\Delta G_{\text{H}^*}$ ).<sup>46</sup> This free energy change serves as a crucial descriptor for understanding the behavior of catalysts during the HER. Achieving optimal values for  $\Delta G_{\text{H}^*}$  is essential, as it directly affects the reaction rate. Specifically, the value of  $\Delta G_{\text{H}^*}$  must be finely tuned; it should not be excessively negative or overly



Fig. 2 Different pathways for the HER (a) in acidic and (b) in alkaline media. Reprinted with permission.<sup>45</sup> Copyright 2023, Wiley-VCH. (c) Mechanism of electrocatalytic HER. Reprinted with permission.<sup>46</sup> Copyright 2018, Wiley-VCH. (d) Atomic model and (e) Schematic energy band diagrams of the  $\text{WS}_2/\text{CoS}_2$  heterostructure in equilibrium; the respective vacuum level ( $E_{\text{vac}}$ ), work function ( $\Phi$ ), conduction band level ( $E_{\text{c}}$ ), valence band level ( $E_{\text{v}}$ ), Fermi level of the metal ( $E_{\text{Fm}}$ ), and Fermi level of the semiconductor ( $E_{\text{Fs}}$ ) are shown. Reprinted with permission.<sup>47</sup> Copyright 2020, American Chemical Society.



positive. A  $\Delta G_{\text{H}^*}$  that is too negative indicates that  $\text{H}^*$  atoms are adsorbed onto the electrode surface with excessive strength, which can lead to a bottleneck effect. This strong binding inhibits the subsequent desorption of  $\text{H}^*$  from the surface, effectively blocking the active sites and diminishing the overall activity of the catalyst. By contrast, a very positive  $\Delta G_{\text{H}^*}$  implies a weak interaction between  $\text{H}^*$  and the electrode material. Such weak binding causes difficulties for  $\text{H}^*$  atoms to adsorb on the surface, which would consequently hinder the overall HER process.<sup>46</sup> For optimal catalysis in the HER,  $\Delta G_{\text{H}^*}$  should be maintained at approximately zero, similar to the behavior observed with Pt. Moreover, interface engineering is essential for controlling the  $\text{H}_2\text{O}$  dissociation barrier, which directly affects  $\text{H}^*$  coverage and the efficiency of the HER. By tailoring interfaces with enhanced electronic characteristics, catalysts can improve  $\text{H}_2\text{O}$  adsorption and encourage charge redistribution that weakens O–H bonds, thereby speeding up  $\text{H}^*$  formation. For instance, metal–metal oxide heterostructures generate localized electric fields that boost electron transfer, lowering the energy needed for  $\text{H}_2\text{O}$  dissociation. Likewise, bimetallic catalysts utilize charge polarization effects to fine-tune  $\Delta G_{\text{H}^*}$ , achieving an optimal balance between the adsorption and desorption of  $\text{H}^*$ . These adjustments at the interface ultimately determine whether the reaction proceeds through the Tafel or Heyrovsky pathway, affecting the overall kinetics and efficiency of the HER.

The electrocatalyst helps to move electrons from the electrode to the reactants and/or promotes chemical transformation, which is represented by an overall half-reaction. Electrocatalytic materials can modify and accelerate electrochemical reactions without being consumed by interacting with reagents to change reaction pathways and lower the activation barrier. For electrochemical reactions, the reaction rate depends on the electric field crossing the electrode/solution interface, which is involved in an electrochemical reaction; the temperature, pressure, solution medium, and state of the solid surface also play a role in determining the reaction rate. Thus, the rate of electrochemical reactions can be regulated by altering the electrocatalyst on the electrode surface. The electron transfer process that occurs at the interface between  $\text{WS}_2$  and  $\text{CoS}_2$ , as depicted in Fig. 2d and e, is a crucial aspect of understanding their electronic interaction.<sup>47</sup> The energy band diagram illustrates the relationship between these two materials in this equilibrium state, and shows distinct work function ( $\phi$ ):  $\text{WS}_2$  (5.89 eV) and  $\text{CoS}_2$  (5.50 eV).<sup>48,49</sup> Owing to this difference in the work function, the Fermi level of  $\text{CoS}_2$ , which is energetically higher than that of  $\text{WS}_2$ , influences the movement of electrons. Specifically, electrons migrate from  $\text{CoS}_2$  to  $\text{WS}_2$ , resulting in the formation of a Schottky barrier at the interface (Fig. 2e).<sup>47</sup> This electron transfer continues until the system stabilizes and reaches a state of equilibrium. As anticipated, this process facilitates electronic modulation of the  $\text{WS}_2/\text{CoS}_2$  heterostructure. More importantly, it leads to an increase in the surface electron density of  $\text{WS}_2$ , enriching its electronic properties and enhancing its potential HER applications.<sup>47</sup> This intricate interplay between the materials highlights their

unique characteristics and underscores the significance of the interface in achieving the desired electronic performance.

The Volmer, Heyrovsky, and Tafel steps are fundamental reactions, each of which occurs at the catalytic interface, where the interaction between the catalyst surface and the reacting species occurs. The efficiency of the HER is highly influenced by this interaction as it determines the effectiveness of hydrogen production. The surface characteristics of the catalyst, such as its electronic structure, crystallinity, and surface energy, are critical factors that influence the strength of adsorption of the reactant species.<sup>50</sup> Variations in the surface energy can affect the ease of hydrogen atom bonding to the catalyst surface. Thus, interface engineering plays a significant role in modulating the surface properties of the catalysts. By altering the catalyst composition or structure, researchers can alter the adsorption strength of key intermediates, thereby influencing the Volmer, Heyrovsky, and Tafel steps. This engineering process involves techniques such as alloying, applying coatings, and physically restructuring the catalyst surface. The interplay between the electron transfer processes, adsorption energy, and stabilization of surface intermediates is vital for optimizing the overall efficiency of the HER. For example, favorable adsorption may enhance the Volmer step (initial protonation of the surface), whereas efficient electron transfer is crucial during the Heyrovsky step (where other hydrogen ions and electrons are involved). The Tafel step, in which hydrogen gas is formed and desorbed from the surface, is also influenced by these factors. Thus, understanding and manipulating these steps through careful design of the catalytic interface is essential for achieving highly efficient hydrogen evolution.

### 3. Strategies for interface-engineered HER electrocatalysts

#### 3.1. Heterostructures

Heterostructures arise by stacking or combining dissimilar materials, and have distinct physical or chemical properties, which give rise to new functionalities that are not exhibited by the individual components. Using different materials, such as combinations of metal–metal hydroxides or oxides ( $\text{M}/\text{M}(\text{OH})_2$  or  $\text{M}/\text{MO}$ ), to form heterostructures is a fundamental technique in the field of materials science.<sup>51,52</sup> Heterostructures comprising metal–metal (hydro) oxides consist of layers of different metals on metal oxides, typically aimed at enhancing properties such as electrical conductivity, magnetic behavior, or catalytic activity. Simple transition-metal oxides made from abundant earth elements (*e.g.*, Ni, Co, Fe, Mo, W, Ti, Mn, Sn, Cu, *etc.*) are predominant within the metal oxide family, including NiO, CoO,  $\text{SnO}_2$ ,  $\text{TiO}_2$ ,  $\text{Fe}_2\text{O}_3$ ,  $\text{MoO}_x$ ,  $\text{WO}_x$ ,  $\text{MnO}_2$ , and  $\text{Cu}_2\text{O}$ , and have been extensively studied as promising candidates for HER electrocatalysis using various methods.<sup>53,54</sup>

Metal (hydro)oxides can effectively facilitate water dissociation, and as such, can promote the Volmer step (*i.e.*, water dissociation) during the alkaline HER process.<sup>55</sup> Nickel-based hydroxides, particularly  $\text{Ni}(\text{OH})_2$ , are widely recognized for their



significant role in catalyzing water dissociation and the formation of reaction intermediates, thereby enhancing the kinetics of the HER.<sup>55,56</sup> An important contributing factor to this enhancement is the modification of the electronic structure associated with the adsorption and desorption energy of intermediates through the development of a heterojunction. Heterostructures based on Ni and Ni(OH)<sub>2</sub> are particularly advantageous, as the heterojunction can be readily created through one-pot synthesis or the partial conversion of metallic nickel to Ni(OH)<sub>2</sub>.<sup>57</sup> Guo *et al.* showcased this concept by fabricating a Ni@Ni(OH)<sub>2</sub> heterostructure catalyst on a titanium paper substrate using a combination of electrodeposition and subsequent electrochemical activation.<sup>58</sup> The electrochemical activation process resulted in the formation of Ni (oxy)hydroxides, leading to surface reconstruction of Ni@Ni(OH)<sub>2</sub>, consequently creating abundant heterojunctions and modulating electrons.

Internal electric fields within heterostructures are essential in modifying the electronic configuration of catalysts by affecting charge distribution and energy level alignment. The electric field at the interface of a heterostructure, such as Ni/Ni(OH)<sub>2</sub>, arises due to charge redistribution between the two components.<sup>59</sup> This occurs because of differences in their work functions and electronic structures, leading to electron transfer across the interface. In the case of Ni/Ni(OH)<sub>2</sub>, the metallic Ni donates electrons to Ni(OH)<sub>2</sub>, establishing an interfacial electric field that orients from the hydroxide layer toward the Ni surface. These fields originate from interfacial polarization, lattice strain, and charge transfer among the various components of the heterostructure. Their influence on the d-band center, a critical indicator of catalytic efficacy can markedly change the adsorption strength of reaction intermediates, thus fine-tuning catalytic performance. In the case of the HER, the internal electric field can alter the d-band center of metal catalysts, impacting the binding strength of hydrogen intermediates (H<sup>\*</sup>). A downshift in the d-band center generally weakens the adsorption of hydrogen, facilitating efficient hydrogen desorption, whereas an upshift strengthens adsorption, which can impede desorption but improve initial activation. For example, creating a RuO<sub>2</sub>/NiRu heterogeneous interface can lead to a downshift in the d-band center of the Ni–Ru catalyst.<sup>60</sup> This modification reduces the adsorption of hydrogen intermediates, thereby improving HER performance in alkaline environments. By carefully engineering heterostructures to optimize these interactions, one can achieve a balance that enhances HER kinetics. Furthermore, the electric field can promote charge transfer, lowering overpotential and increasing reaction rates. This foundational knowledge allows for the methodical design of high-performance electrocatalysts with adjustable electronic configurations for HER.

Combining metal (hydro)oxides with conventional HER electrocatalysts effectively creates high-performance alkaline HER electrocatalysts. Following this trend, Ni(OH)<sub>2</sub> supported by NF with Ru Nanoparticles (NPs) was fabricated as a self-supported material using the method of “spontaneous oxidation–reduction reaction”.<sup>61</sup> The interaction between metallic

Ru and Ni(OH)<sub>2</sub> can lead to an improved HER activity owing to the collaborative effect that is recognized as a synergistic phenomenon. The heterostructure interaction between the metal and metal (hydro)oxide facilitates electron transfer from the metal to metal (hydro) oxide, leading to optimization of the hydrogen adsorption energy.

Structural engineering is essential for two-dimensional (2D) heterostructures to achieve electrical modulation, which can maximize their internal activity toward the HER. The excellent versatility in adjusting the electrocatalytic activity was provided by the 2D heterostructures. Li *et al.* presented a facile bottom-up approach to fabricating WS<sub>2</sub>/W heterojunction electrodes (Fig. 3a and b).<sup>62</sup> W foil was oxidized in the air to form WO<sub>3</sub>/W with a larger surface area, followed by sulfurization of WO<sub>3</sub>/W in Ar and H<sub>2</sub>, during which process, vertical WS<sub>2</sub> flakes were synthesized in the W substrate (Fig. 3c–e). Researchers combined a 2D MoSe<sub>2</sub> thin flake with a MoS<sub>2</sub> nanosheet and synthesized the MoSe<sub>2</sub>/MoS<sub>2</sub> heterostructure through heterojunction engineering and an epitaxial growth process.<sup>63</sup> The MoSe<sub>2</sub>/MoS<sub>2</sub> heterostructure which comprised abundant interfaces enabled more exposed edge sites for electrochemical reaction and facilitated charge transport with the open porous space, which arose from the synergistic effect through the combination of MoS<sub>2</sub> and MoSe<sub>2</sub>. Similarly, Sun *et al.* designed a flower-like WS<sub>2</sub>/WSe<sub>2</sub> heterostructure by heterojunction engineering through a solvothermal process (Fig. 3f).<sup>64</sup> The researchers regulated the sphere-like morphology into a flower-like morphology by optimizing the reaction process (~5–12 h). The flower-like morphology of WS<sub>2</sub>/WSe<sub>2</sub> was 5 nm thick and 200 nm wide, with diameters ranging from 700 nm to 900 nm (Fig. 3g–i).<sup>64</sup> The synergistic effect of the combination of WS<sub>2</sub> and WSe<sub>2</sub> generated abundant interfaces, as observed in the HRTEM images.

Han *et al.* developed ReS<sub>2</sub>@NiFe-LDH/carbon fiber paper (CFP) hetero-nanosheets using a two-step hydrothermal technique, as illustrated in Fig. 4a.<sup>65</sup> The NiFe-LDH nanosheets were evenly distributed on the surface of ReS<sub>2</sub>, and the hetero-interfaces were visible in the SEM image (Fig. 4b). As shown in Fig. 4c, ReS<sub>2</sub>, which measures between 100 and 150 nm in lateral size, effectively supports the vertically oriented NiFe-LDH nanosheets (indicated by the white dashed line), corroborating the FE-SEM findings (Fig. 4b). Fig. 4d presents the polarization curves demonstrating the electrocatalytic HER performance of the ReS<sub>2</sub>/NiFe-LDH hybrids, indicating an overpotential of just 101 mV at 10 mA cm<sup>-2</sup>.<sup>65</sup> This overpotential (101 mV) is lower than that of ReS<sub>2</sub> (133 mV) and NiFe-LDH (375 mV) and comparable to that of the 20% Pt/C catalyst (11 mV, Fig. 4d). The ReS<sub>2</sub>/NiFe-LDH hybrids display a significantly smaller Tafel slope of 81 mV dec<sup>-1</sup> (Fig. 4e) compared with that of ReS<sub>2</sub> (122 mV dec<sup>-1</sup>) and NiFe-LDH (109 mV dec<sup>-1</sup>), suggesting a synergistic effect that arises from the strong interface between NiFe-LDH and ReS<sub>2</sub>. In addition, the ReS<sub>2</sub>/NiFe-LDH hybrids demonstrated excellent stability for the HER over 30 h at current densities of 50, 100, and 200 mA cm<sup>-2</sup> (Fig. 4f).<sup>65</sup> The researchers noted the exceptional activity of the ReS<sub>2</sub>/NiFe-LDH heteronanosheets for the HER, which resulted





**Fig. 3** (a) Schematic illustrating  $\text{WS}_2$  synthesis process. (b) Structural diagram of  $\text{WS}_2/\text{W}$ . Scanning electron microscope (SEM) image of (c)  $\text{WO}_3$  and (d)  $\text{WS}_2$  nanosheets on W foil. (e) Side-view SEM image of  $\text{WS}_2/\text{W}$ . Reprinted with permission.<sup>62</sup> Copyright 2019, Elsevier. (f) Schematic illustration of the synthesis of the flower-like  $\text{WS}_2/\text{WSe}_2$  heterostructure, (g) SEM image, (h) high resolution transmission electron microscope (HRTEM) image, and (i) high-angle annular dark-field scanning transmission electron microscope (HAADF-STEM) image of flower-like  $\text{WS}_2/\text{WSe}_2$  heterostructure and energy dispersive X-ray spectroscopy (EDX) elemental mappings image. Reprinted with permission.<sup>64</sup> Copyright 2022, Elsevier.

from the S–O bonds present at the heterointerfaces between NiFe-LDH and  $\text{ReS}_2$ , as well as the strong coupling effect and vertical arrangement of NiFe-LDH and  $\text{ReS}_2$ .

Jiang *et al.* devised a heterostructure approach to modify the electronic configuration of the active site and facilitate surface reconstruction by creating Co–Ni–B heteronanosheets on reduced graphene oxide (Co–Ni–B/RGO).<sup>66</sup> The Co–Ni–B/RGO was produced by reducing a solution of metal salts and graphene oxide using sodium borohydride (Fig. 4g). Fig. 4h indicates that the Co–Ni–B/RGO catalysts with graphene substrates display a consistent arrangement of nanosheets.<sup>66</sup> The effective interaction between graphene and the boride nanosheets prevents agglomeration of the nanosheets and contributes to better dispersion, enhancing the active surface area of the Co–Ni–B/RGO catalyst. The TEM image of Co–Ni–B/RGO clearly shows that the Co–Ni–B nanosheets are firmly attached to the graphene substrate; the nanosheet sizes range between 20–30 nm (Fig. 4i). The HRTEM image of Co–Ni–B/RGO, shown in Fig. 4j, indicates that the lattice fringes can be

indexed to the (211) planes of  $\text{Co}_2\text{B}$  and  $\text{Ni}_2\text{B}$ , respectively, and a noticeable interface exists between  $\text{Co}_2\text{B}$  and  $\text{Ni}_2\text{B}$ .<sup>66</sup> The Co–Ni–B/RGO displays catalytic performance for the HER with an overpotential of 131 mV at a current density of  $10 \text{ mA cm}^{-2}$  (Fig. 4k), significantly lower than that of Co–Ni–B (200 mV), Co–B/RGO (249 mV), Ni–B/RGO (298 mV), and RGO (565 mV). Consequently, the Tafel plots of the aforementioned samples reveal a consistent trend in the HER kinetics (Fig. 4l).<sup>66</sup> Co–Ni–B/RGO features a low Tafel slope of  $86 \text{ mV dec}^{-1}$ , which is less than those of Co–Ni–B ( $98 \text{ mV dec}^{-1}$ ), Co–B/RGO ( $107 \text{ mV dec}^{-1}$ ), Ni–B/RGO ( $140 \text{ mV dec}^{-1}$ ), and RGO ( $170 \text{ mV dec}^{-1}$ ).<sup>66</sup> The Tafel slope value for Co–Ni–B/RGO suggests that hydrogen evolution in alkaline conditions may proceed *via* the Volmer–Heyrovsky mechanism, with the Heyrovsky step being the rate-determining factor. The notably lower Tafel slope of Co–Ni–B/RGO compared with those of Co–B/RGO and Ni–B/RGO indicates favorable HER kinetics for  $\text{H}_2\text{O}$  dissociation and  $\text{H}_2$  production. For the Co–Ni–B/RGO heterostructures, the reverse electron transfer from boron resulted in an enhanced electron density around the metal site,





**Fig. 4** (a) Schematic illustration of synthesis process, (b) field emission scanning electron microscope (FE-SEM) image, (c) TEM image of the  $\text{ReS}_2/\text{NiFe}$ -layered double hydroxide (LDH) heteronanosheets, (d) HER polarization curves, and (e) polarization curve-derived Tafel slopes of the  $\text{ReS}_2/\text{NiFe}$ -LDH heteronanosheets,  $\text{NiFe}$ -LDH,  $\text{ReS}_2$ , and 20% Pt/C in Ar-saturated 1 M KOH solution, (f) Chronopotentiometry curves of the  $\text{ReS}_2/\text{NiFe}$ -LDH heteronanosheets at various current densities of 50, 100, and 200  $\text{mA cm}^{-2}$ , respectively. Reprinted with permission.<sup>65</sup> Copyright 2021, American Chemical Society. (g) Schematic illustration for the Co–Ni–B/reduced graphene oxide (RGO) fabrication, (h) SEM image, (i) TEM, (j) HRTEM of Co–Ni–B/RGO, (k) HER polarization curves, and (l) corresponding Tafel plots of Co–Ni–B/RGO compared with those of RGO, Co–B/RGO, Ni–B/RGO, Co–Ni–B, and Pt/C. Reprinted with permission.<sup>66</sup> Copyright 2024, Elsevier.

positively impacting the HER. Additionally, graphene serves as an excellent conductor, effectively lowering the interfacial barrier for electron transfer and thus accelerating the reaction kinetics.

In addition to the main findings, a comprehensive summary of the relevant literature on the formation of heterostructures is presented in Table 1. Table 1 highlights various studies that have focused on the interface engineering strategies used, as well as the specific synthesis processes used to create these catalysts. Furthermore, the table details the performance of the catalysts in terms of the HER overpotential when immersed in an electrolyte solution. This systematic overview aims to provide clearer insights into the effectiveness of different approaches for enhancing catalyst performance for HER applications.

### 3.2. Core-shell architectures

Core-shell nanostructures represent a significant advancement in the field of interface engineering, particularly for enhancing the electrochemical properties for various applications. At the

nanoscale, these structures consist of a distinct central core enveloped by an additional layer, referred to as the shell, which is composed of different materials.<sup>101,102</sup> The unique characteristics of the core-shell nanoparticles are intricately linked to the specific composition, arrangement, and structural organization of both the core and shell, as well as the interactions occurring at their interface. The evolution of core-shell nanostructures plays a pivotal role in maximizing the exposure of active surface areas, which is essential for improving electrochemical reactions.<sup>103</sup> By carefully manipulating the electronic and chemical properties at interfacial sites, researchers can achieve enhanced performance across multiple core and shell surfaces. Moreover, one of the critical advantages of these nanostructures is their ability to improve long-term durability, particularly in highly corrosive electrolyte environments, owing to the protective attributes provided by robust and well-engineered shell layers.<sup>104</sup> These core-shell nanostructures can manifest in various geometric configurations, including



Table 1 Comparison of reported HER catalysts developed through interface engineering strategies

| Catalyst   | Interface engineering strategies     | Synthesis method                                      | HER $-\eta$ (@ 10 mA cm <sup>-2</sup> ) | Electrolyte   | Ref. |
|--|--------------------------------------|---|---|---|------|
| Cu@WC  | Core-shell structure                 | Chemical oxidation, magnetron sputtering              | 92, 119, 173 mV                         | 0.5 M H <sub>2</sub> SO <sub>4</sub> , 1 M KOH, 1 M PBS     | 67   |
| MoSe <sub>2</sub> /Mo                                      | Core-shell structure                 | GLAD process & plasma-assisted selenization           | 166 mV                                  | 0.5 M H <sub>2</sub> SO <sub>4</sub>                        | 68   |
| NiS <sub>2</sub> -MoS <sub>2</sub>                         | Core-shell structure                 | Solvothermal & CVD-sulfurization                      | 76 mV                                   | 1 M KOH   | 69   |
| Coalesced-type V-MoS <sub>2</sub>                          | Heteroatom-doping, vacancy defect    | Chemical vapor deposition                             | 100 mV                                  | 0.5 M H <sub>2</sub> SO <sub>4</sub>                        | 70   |
| V-MoS <sub>2</sub> /Cu                                     | Heteroatom-doping, vacancy defect    | Chemical vapor deposition                             | 80 mV                                   | 0.5 M H <sub>2</sub> SO <sub>4</sub>                        | 71   |
| P-1T-CMS@CC  | Heteroatom-intercalation & doping    | Hydrothermal reaction                                 | 95 mV                                   | 1 M KOH   | 72   |
| CoTe <sub>2</sub> -WTe <sub>2</sub>                        | Heteroatom-doping                    | Hydrothermal reaction                                 | 178 mV                                  | 1 M KOH   | 73   |
| Ni/WO <sub>x</sub> /NF                                     | Anion exchange/vacancy defect        | Hydrothermal process, H <sub>2</sub> -reduction       | 42 mV                                   | 1 M KOH   | 74   |
| ReSe <sub>2</sub> -VSe <sub>2</sub>                        | Alloy strategy                       | Hot injection colloidal reaction                      | 77 mV                                   | 0.5 M H <sub>2</sub> SO <sub>4</sub>                        | 75   |
| Ni-Co-Mn-P (NCMP)/NF                                       | Alloy strategy                       | Electrosynthesis                                      | 100 mV                                  | 1 M KOH   | 76   |
| RhP <sub>x</sub> /CoNiP <sub>4</sub> O <sub>12</sub> /CC   | Heteroatom-doping                    | Co-precipitation, ion exchange, & phosphorylating     | 30 mV                                   | 1 M KOH   | 77   |
| CoP/Ti <sub>3</sub> C <sub>2</sub> MXene                   | Heterostructure                      | Exfoliation, phosphorization                          | 102, 71, and 124 mV                     | 1 M KOH, 0.5 M H <sub>2</sub> SO <sub>4</sub> , 1 M PBS     | 78   |
| Ni <sub>2</sub> P/MoO <sub>2</sub> /NF                     | Heterostructure                      | Hydrothermal process, phosphorization                 | 34 mV                                   | 1 M KOH   | 79   |
| Mo <sub>0.7</sub> W <sub>0.3</sub> N <sub>1.2</sub>        | Heterostructure                      | Catalytic molten salt method                          | 122 mV                                  | 1 M KOH   | 80   |
| Ni <sub>3</sub> N-Co <sub>3</sub> N NAs/NF                 | Anion exchange/hetero-interface      | Hydrothermal process, annealing treatment             | 43 mV                                   | 1 M KOH   | 81   |
| CoMoN <sub>x</sub> -500 NSAs/NF                            | Heteroatom-doping/hetero-structures  | Hydrothermal, CVD-nitridation                         | 91 mV                                   | 1 M KOH   | 82   |
| Fe <sub>2</sub> P/Co <sub>2</sub> N                        | Heteroatom-doping, hetero-structures | Electrodeposition, CVD-nitridation & -phosphorization | 29 mV                                   | 1 M KOH   | 83   |
| Mo <sub>2</sub> N-Co <sub>x</sub> N-5                      | Heteroatom-doping, hetero-structures | Hydrothermal, CVD-nitridation                         | 29 mV                                   | 1 M KOH   | 84   |
| Co <sub>6</sub> W <sub>6</sub> C@NC/CC                     | Heteroatom doping                    | MOF-derived synthesis                                 | 59 mV                                   | 1 M KOH   | 85   |
| Ir-NiMoP-NiMoP <sub>x</sub> O <sub>y</sub> /CNTs-Gr/Cu     | SA-doping/heterostructure            | Electrodeposition, impregnation, and phosphorization  | 90 mV                                   | 1 M KOH   | 86   |
| Ni <sub>3</sub> Fe-CO <sub>3</sub> <sup>2-</sup> LDH-Pt SA | Alloy structure/SA-doping            | Anion exchange and electroreduction                   | 45 mV                                   | 1 M KOH   | 87   |
| Pt SASS/AG   | SA-doping                            | Aniline anchoring and microwave reduction             | 12 mV                                   | 0.5 M H <sub>2</sub> SO <sub>4</sub>                        | 88   |
| Fe-SAC C-Ni@3  | SA-doping                            | MOF-assisted Electrodeposition                        | 164 mV                                  | 1 M KOH   | 89   |
| Pt <sub>SA</sub> -Mn <sub>3</sub> O <sub>4</sub>           | SA-doping                            | Electrodeposition                                     | 24 mV                                   | 1 M KOH   | 90   |
| Ir@TiO <sub>2</sub>  | SA-doping                            | Thermolysis and <i>in situ</i> deposition             | 41 mV                                   | 0.5 M H <sub>2</sub> SO <sub>4</sub>                        | 91   |
| Ru <sub>SA</sub> @CoP <sub>x</sub> -350                    | Heterostructure                      | Hydrothermal method, impregnation, and phosphidation  | 26 mV                                   | 1 M KOH   | 92   |
| (Ru-N)@Pt  | SA-doping and alloy structure        | Wet chemistry and annealing                           | 15 mV                                   | 1 M KOH   | 93   |
| Pt <sub>at</sub> -CoP MNSs/CFC                             | SA-doping                            | Electrodeposition and phosphorization                 | 13 mV                                   | 1 M KOH   | 94   |
| RuNi@rGO   | SA-alloy structure                   | Wet chemistry   | 15 mV                                   | 1 M KOH   | 95   |
| Ni <sub>5</sub> P <sub>4</sub> -Ru                         | SA-doping and heterostructure        | Wet chemistry and annealing                           | 123 mV                                  | 1 M KOH   | 96   |
| Rh <sub>1</sub> -TiC                                       | SA-doping                            | Incipient wetness method and annealing                | 22 mV                                   | 0.5 M H <sub>2</sub> SO <sub>4</sub>                        | 97   |
| NiCo-SAD-NC  | Alloy                                | Precipitation and annealing                           | 61 and 54.7 mV                          | 1 M KOH and 0.5 M H <sub>2</sub> SO <sub>4</sub>            | 98   |
| Ru <sub>0.10</sub> @2H-MoS <sub>2</sub>                    | Doping & phase engineering           | Hydrothermal method                                   | 51, 168, and 137 mV                     | 1 M KOH, 0.5 M H <sub>2</sub> SO <sub>4</sub> , and 1 M PBS | 99   |
| 5Pt/VSe <sub>2</sub> /CP                                   | SA-doping                            | Hydrothermal method                                   | 77 mV                                   | 0.5 M H <sub>2</sub> SO <sub>4</sub>                        | 100  |

one-dimensional (1D) nanorods or nanowires, 2D nanosheets, and three-dimensional (3D) framework structures. Depending on the intended application, shells can be fabricated from a

diverse array of organic or inorganic materials.<sup>105</sup> The structural diversity of core-shell configurations allows for extensive opportunities to tailor their properties. This tailoring can be



achieved by meticulously controlling the chemical composition, relative dimensions, and specific morphologies of both the core and shell components.

In practical applications, core-shell nanostructures have been successfully utilized in the development of a wide range of noble-metal-free electrocatalysts. Such electrocatalysts have demonstrated performance metrics that are comparable to or even surpass those of traditional noble-metal-based catalysts, highlighting the potential of core-shell architectures for sustainable and efficient electrochemical applications. Materials composed of tungsten carbide (WC) display electronic structures akin to those of Pt near the Fermi level. Scientists have created nanowires featuring a core-shell design with Cu and WC, aiming to merge the electrical conductivity of Cu with the catalytic properties of WC for the HER.<sup>67</sup> The interaction between WC and Cu in the core-shell configuration modified the atomic and electronic characteristics of WC, diminishing the hydrogen bond strength during absorption, and ultimately enhancing the efficiency of the HER. The core-shell arrangement of Cu@WC was found to boost the carrier density in WC, with interfacial electrons becoming significantly delocalized when subjected to an external electric field. Additionally, the closely aligned work functions (WF) of Cu and WC maintain a high concentration of Pt-like electrons in WC.<sup>67</sup>

1D hierarchical core-shell nanostructures have garnered significant interest in the field of materials science owing to their advantageous characteristics. These structures are particularly appealing because they have large surface areas with numerous active sites, which can enhance various chemical reactions and yield improved performances in various applications. In addition, the efficient electron transport properties observed in these nanostructures, even at the nanometer scale, render them ideal for electronic and energy-related applications. In a recent study, Yu *et al.* innovatively integrated 1D Cu nanowires (NWs) with two-dimensional cobalt iron layered double hydroxide (CoFe LDH) nanosheets (NSs) to create a novel hierarchical core-shell nanoarchitecture.<sup>106</sup> This remarkable composite structure is built on the foundation of copper foams, which serve as a robust substrate as shown in Fig. 5a.<sup>106</sup> The diameter of the core-shell hybrid was approximately 1  $\mu\text{m}$ , with a core of Cu NWs measuring approximately 200 nm and a CoFe LDH nanosheet shell of approximately 400 nm as shown in Fig. 5b.<sup>106</sup> The design leverages the high conductivity and structural integrity of the Cu nanowires and capitalizes on the unique electrochemical properties of the CoFe LDH nanosheets. By combining these two components, researchers aim to enhance the overall performance of nanostructures for the HER.

Recent studies have indicated that Ru with a face-centered cubic (fcc) structure generally exhibits superior electrocatalytic performance compared with that of its hexagonal close-packed (hcp) counterpart, particularly in HER reactions.<sup>108</sup> This superior performance in the fcc configuration is attributed to its unique electronic properties and active sites that facilitate more efficient electrochemical reactions. However, a significant challenge arises because Ru predominantly crystallizes in the hcp

crystal phase in its natural form.<sup>109</sup> This prevalence of the hcp structure over the fcc structure has created a complex situation for researchers aiming to synthesize fcc-structured Ru-based catalysts. The synthesis of these catalysts is crucial for improving their application in electrocatalysis; however, it remains a considerable challenge because of the difficulty in stabilizing the fcc phase and achieving the desired crystalline properties during the manufacturing process. The development of the bimetallic Pd@Ru core-shell structure has emerged as an effective method to address this issue through the epitaxial growth of an fcc Ru shell on the surface of the fcc Pd core.<sup>107</sup> Furthermore, in contrast to Ru oxides, which are semiconductors that tend to exhibit low conductivity and metallic characteristics, this is detrimental to the electrocatalytic process.

A nonmetal such as P, which has an electronegativity value similar to those of Pd or Ru, can donate extra electrons to improve electron delocalization and conductivity in ruthenium-based catalysts and can alter the d-band center to create an appropriate affinity for H\*, thereby enhancing the kinetics of the HER.<sup>110</sup> Thus, Ding *et al.* developed core-shell Pd@RuP nanorods *via* epitaxial growth where the ultrathin RuP layers expand the fcc crystal structure and (111) plane of the core Pd nanorods (Fig. 5c).<sup>107</sup> The high degree of lattice matching can be attributed to the comparable atomic radii of Pd and Ru and the templating influence of the Pd NRs that act as growth seeds. By contrast, the clearly defined interplanar distances between the Pd (111) core and Ru (111) shell in Pd@RuP NRs are increased to 2.22 Å (red square, Fig. 5d(1)) and 2.29 Å (green square, Fig. 5d(2)), respectively, when compared with the corresponding regions in Pd@Ru NRs.<sup>107</sup> The increased lattice fringe spacings of the Ru (111) shell in Pd@RuP nanorods can be attributed to the successful incorporation of phosphorus. Thus, the Pd@RuP NRs demonstrated better electrocatalytic stability and enhanced activity compared with those of Pd@Ru NRs and Pt/C and achieved a low overpotential of 18 mV at 10 mA cm<sup>-2</sup> during the alkaline HER process.<sup>107</sup>

Qu *et al.* described the growth of Mo hierarchical nanostructures, such as nanorods, nanoscrews, and nanohelices, on a Mo/glass substrate through a Glancing angle deposition (GLAD) process, followed by a plasma-assisted selenization technique.<sup>68</sup> Therefore, core-shell 3D-hierarchical nanostructures of MoSe<sub>2</sub>/Mo can be created on a conductive Mo substrate, making it an advantageous configuration for an electrocatalytic electrode intended for hydrogen evolution. In this setup, several monolayers of shell-MoSe<sub>2</sub> function as active catalysts with increased surface areas, while the Mo core facilitates rapid electron transfer to the underlying conductive layer of Mo.

The shapes of the Mo hierarchical structures that were developed can be altered by adjusting a ratio defined by  $\rho = r/\Delta\phi$ , where  $r$  represents the deposition rate and  $\Delta\phi$  indicates the rotational speed of the substrate. As illustrated in Fig. 5e, nano helices, nanoscrews, and nanorods were produced by varying  $\Delta\phi$  between 0.25, 0.5, and 2 deg s<sup>-1</sup> while maintaining a constant deposition rate ( $r = 0.1 \text{ nm s}^{-1}$ ), resulting in  $\rho$  values of 144, 72, and 18 nm rev<sup>-1</sup>, respectively.<sup>68</sup> Owing to the





Fig. 5 (a) Fabrication process and (b) TEM image of Cu@CoFe LDH core-shell nanostructure electrocatalysts. Reprinted with permission.<sup>106</sup> Copyright 2017, Elsevier. (c) Schematic of the preparation of nanorods, (d) HRTEM image, and (d1)–(d3) corresponding integrated pixel intensities of Pd@RuP nanorods (NRs). Reprinted with permission.<sup>107</sup> Copyright 2023, Elsevier. (e) Cross-section SEM images of nanohelices, nanoscrews, and nanorods deposited at substrate rotation speeds of  $\Delta\phi = 0.25, 0.5,$  and  $2 \text{ deg s}^{-1}$ , respectively, corresponding to  $\rho = 144, 72,$  and  $18 \text{ nm rev}^{-1}$ ; the scale bar is 250 nm and (f) Scan-rate dependence of the current density at  $E = 0.3 \text{ V}$  versus RHE for the three different Mo hierarchical nanostructures. Reprinted with permission.<sup>68</sup> Copyright 2016, Wiley-VCH.

comparatively coarse texture of Mo/glass, the double-layer capacitances ( $C_{dl}$ ) of  $1.495 \text{ mF cm}^{-2}$  obtained from flat Mo is greater than that anticipated for a flat electrode (usually in the range of tens of  $\mu\text{F cm}^{-2}$ ) (Fig. 5f). The development of Mo 3D-hierarchical structures on Mo/glass leads to a more than four-fold increase in capacitance. Notably, the highest capacitance was measured from the Mo nanoscrews ( $C_{dl}$  of  $6.855 \text{ mF cm}^{-2}$ ), which is approximately 4.6 times greater than that of flat Mo.<sup>68</sup> Shell-MoSe<sub>2</sub> monolayers serve as effective catalysts owing to their increased surface area, while the core Mo enables a rapid electron transfer pathway to the underlying Mo conductive layer.

Wang *et al.* synthesized Co@CoO core/shell nanowire arrays using a simple hydrothermal deposition and hydrogen

reduction technique (Fig. 6a and b).<sup>111</sup> The Co@CoO core/shell nanowire arrays exhibit a slightly curved form and comprise many nodules measuring between 50–70 nm, resulting in a significantly rougher surface texture. Numerous nanopores are present among these nanoparticles, formed by the *in situ* release of vapor and CO<sub>2</sub> from the decomposition of Co<sub>2</sub>(OH)<sub>2</sub>CO<sub>3</sub> during thermal processing (Fig. 6c).<sup>111</sup> This open porous architecture enhances the close interaction between the electrolyte and electrocatalyst, facilitating the efficient release of hydrogen during the HER. The pore size distribution (PSD) derived from the adsorption-desorption curve are also indicating that the Barrett-Joyner-Halenda (BJH) average pore diameter of the Co@CoO core/shell nanowire arrays reveals a characteristic size of approximately 6.54 nm.<sup>111</sup> Notably, the



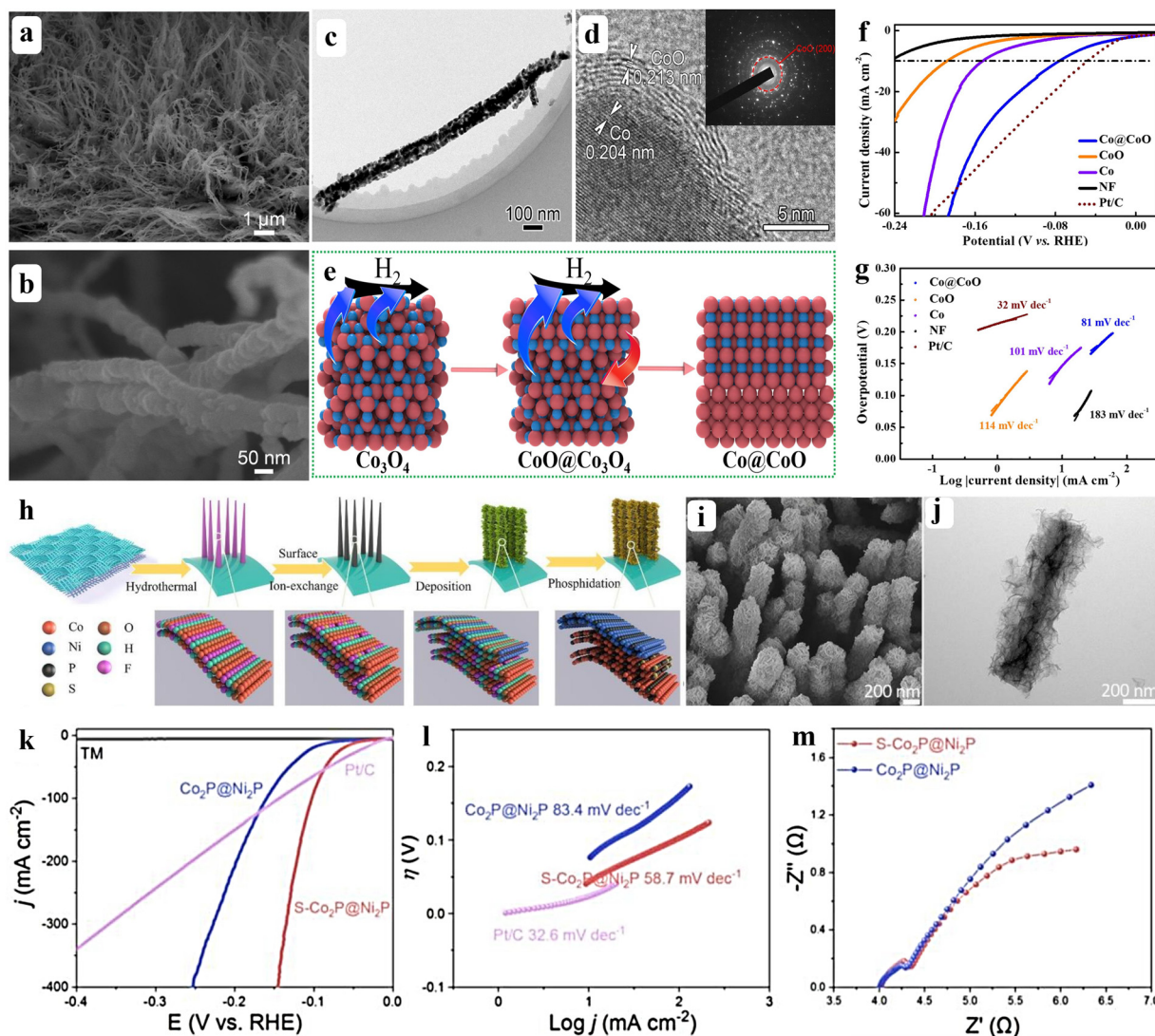


Fig. 6 High-resolution SEM images of (a) and (b) Co@CoO/NF nanowire arrays, TEM-HRTEM images of (c) and (d) Co@CoO nanowire arrays, (e) formation mechanism schematics of Co@CoO; the red and blue atoms represent Co and O atoms, respectively, HER performances: (f) linear sweep voltammetry curves at a scan rate of  $5 \text{ mV s}^{-1}$ ; (g) Tafel plots. Reprinted with permission.<sup>111</sup> Copyright 2022, Elsevier. (h) Schematic illustration of the synthesis of S-Co<sub>2</sub>P@Ni<sub>2</sub>P core@shell heterostructure, (i) SEM image, and (j) TEM image of S-Co<sub>2</sub>P@Ni<sub>2</sub>P, (k) Linear sweep voltammetry (LSV) curves, (l) Tafel slopes, and (m) Nyquist plots of S-Co<sub>2</sub>P@Ni<sub>2</sub>P, Co<sub>2</sub>P@Ni<sub>2</sub>P, Pt/C, and Ti mesh in 1.0 M KOH. Reprinted with permission.<sup>112</sup> Copyright 2022, Elsevier.

nanowires exhibit a distinct core-shell configuration. The core-shell structure is distinctly observable in the high-resolution TEM image (Fig. 6d); the shell thicknesses range between 5–10 nm.<sup>111</sup> Wang *et al.* proposed a synthesis mechanism for Co@CoO core/shell nanowires (Fig. 6e). Initially, the Co<sub>3</sub>O<sub>4</sub> nanowire surface is reduced to CoO, whereas the interior remains as Co<sub>3</sub>O<sub>4</sub> owing to limited H<sub>2</sub> access. Hydrogen reduction causes the internal oxygen atoms to diffuse out, resulting in the conversion of the interior of the nanowire to Co metal, whereas the outer CoO shell persists because of the short reduction duration.

The diffusion of the internal oxygen atoms creates high-energy lattice defects, prompting Co atom migration to these sites which leads to a nodule-like shape. With prolonged reduction, all oxides are converted to Co metal, which

aggregates at high-energy sites and forms a flower-like structure.<sup>111</sup> The CoO/NF and Co/NF catalysts require overpotentials of 191 and 153 mV, respectively, to achieve a current density of  $10 \text{ mA cm}^{-2}$  (Fig. 6f). By contrast, the Co@CoO/NF catalyst displays a significantly reduced overpotential of 76 mV after short-term hydrogen treatment, just 28 mV higher than that of the Pt/C reference (Fig. 6f).<sup>111</sup> Additionally, the Co@CoO/NF has the lowest Tafel slope of  $81 \text{ mV dec}^{-1}$ , outperforming Ni foam, CoO, and Co electrodes, indicating superior HER kinetics (Fig. 6g).<sup>111</sup> The rate-limiting step for the Co@CoO/NF electrode is the Volmer reaction, with the HER process following the Volmer-Heyrovsky pathway.

Yuan *et al.* fabricated a core@shell heterostructure consisting of S-Co<sub>2</sub>P coated with Ni<sub>2</sub>P.<sup>112</sup> The creation of cobalt phosphide nanowires with nickel phosphide nanosheets in a



core@shell structure with sulfur doping (S-Co<sub>2</sub>P@Ni<sub>2</sub>P) involves two main steps: first, sulfur is introduced at the interface of the hydroxide precursor using hydrothermal, ion exchange, and chemical deposition methods. This is followed by phosphidation, transforming the hydroxide into a sulfur-doped phosphide heterostructure (Fig. 6h).<sup>112</sup> SEM analysis indicates that phosphidation maintains the structure of the nanowires with nanosheet arrays (Fig. 6i). The TEM analysis reveals that the inner Co<sub>2</sub>P nanowire surface is uniformly covered with thin Ni<sub>2</sub>P nanosheets (Fig. 6j). The S-Co<sub>2</sub>P@Ni<sub>2</sub>P heterostructure exhibits superior HER activity compared with that of Co<sub>2</sub>P@Ni<sub>2</sub>P and even exceeds that of Pt/C at high current densities (Fig. 6k).<sup>112</sup> The Tafel slopes are 58.7 mV dec<sup>-1</sup> for S-Co<sub>2</sub>P@Ni<sub>2</sub>P and 83.4 mV dec<sup>-1</sup> for Co<sub>2</sub>P@Ni<sub>2</sub>P, indicating faster reaction kinetics for S-Co<sub>2</sub>P@Ni<sub>2</sub>P despite both following a Volmer–Heyrovsky mechanism (Fig. 6l). Additionally, S-Co<sub>2</sub>P@Ni<sub>2</sub>P has a smaller charge transfer resistance ( $R_{ct}$ ) than that of Co<sub>2</sub>P@Ni<sub>2</sub>P, enhancing electron transfer and HER kinetics (Fig. 6m).<sup>112</sup> The literature discussing core–shell catalysts for HER is summarized in Table 1.

### 3.3. Phase engineering

The strategic manipulation of various crystalline phases plays a crucial role in optimizing catalytic properties within the fields of materials science and catalysis. Crystalline phases refer to the specific and ordered arrangements of atoms within a solid material. Each crystalline phase is characterized by unique properties arising from differences in the atomic bonding, symmetry, and overall lattice structure of the material.<sup>113</sup> These variations in crystalline structure can significantly influence the interaction of the material with the reactants, as well as its activity, selectivity, and stability as a catalyst. For example, different bond lengths and angles in various phases can affect the adsorption of reactants on the catalyst surface and how the reaction pathways are facilitated.<sup>114</sup> Additionally, the symmetry of a crystal can influence its electronic properties, which in turn can have profound effects on catalytic performance. By carefully selecting and manipulating these distinct phases through temperature control, pressure adjustment, or chemical treatments, researchers can tailor the catalytic characteristics to meet specific application needs. Therefore, understanding and leveraging the unique catalytic properties associated with different crystalline phases are essential for developing more efficient and effective catalysts for a variety of chemical reactions.

The two-dimensional structure of molybdenum disulfide (MoS<sub>2</sub>) comprises a single Mo atom symmetrically encased by two S atoms, forming S–Mo–S triatomic layers. This unique configuration allows for various arrangements of S atoms, resulting in polymorphisms in MoS<sub>2</sub>. The two primary crystallographic phases exhibit distinctly different electronic characteristics: the semiconducting D<sub>3h</sub>-trigonal prismatic 2H-phase and metallic O<sub>h</sub>-octahedral 1T-phase.<sup>72,115</sup> However, the 2H phase, which is the most thermodynamically stable configuration, has semiconducting properties. Additionally, its basal planes are largely inactive when it comes to catalyzing HER.<sup>116</sup>

By contrast, the metastable 1T-phase displays remarkable metallic conductivity akin to that of metals and features highly active basal planes that make it valuable for catalytic applications. However, this phase is inherently unstable, which poses challenges for its practical use.<sup>116</sup>

The interface plays a crucial role in shaping the phase structure of catalysts for the HER by inducing strain-driven phase changes, stabilizing metastable phases, and altering crystallinity to improve catalytic performance. For instance, in 2D TMDs such as MoS<sub>2</sub>, interfacial interactions can facilitate a transition from the semiconducting 2H phase to the metallic 1T phase, which exhibits higher conductivity and increased active sites for HER.<sup>117</sup> Interfaces also play a crucial role in stabilizing the metastable phases, preventing them from reverting to less effective states. Moreover, by manipulating the interface, one can create localized disorder, which reveals additional active sites and enhances charge transfer.<sup>118</sup> In composite catalysts, heterostructures are designed to optimize phase stability and electronic characteristics, thereby boosting HER performance. Additionally, having an interface can reduce the energy barrier associated with temperature-induced phase transitions, ensuring catalytic effectiveness during operation. Introducing dopants or impurities into the crystal lattice can enhance the stability of specific phases. Sun *et al.* described an easy and scalable N<sub>2</sub>-plasma method to facilitate the phase change of multilayered MoS<sub>2</sub> nanosheets (Fig. 7a) from the 2H to the 1T phase and the existence of both 2H and 1T phases, as shown in Fig. 7(b and c).<sup>119</sup> The researchers achieved an impressive phase conversion rate of approximately 62%; furthermore, the plasma treatment aids in the migration of Pt atoms into the MoS<sub>2</sub> nanosheets, which further increases the yield of the 1T phase to approximately 87% (Fig. 7d).<sup>119</sup> XRD analysis of the pristine MoS<sub>2</sub> nanosheets revealed clearly defined peaks at 14° and 33°, which can be attributed to the (002) and (100) planes of the 2H phase, respectively (Fig. 7e).<sup>119</sup> Conversely, the (002) planes of the N–MoS<sub>2</sub> and N,Pt–MoS<sub>2</sub> nanosheets shifted to lower degrees, indicating a larger interlayer spacing (increased from 6.4 to 6.7 Å for N–MoS<sub>2</sub> and from 6.4 to 6.9 Å for N,Pt–MoS<sub>2</sub>), which corresponded with TEM observations (Fig. 7a).

Subsequently, in the Raman spectra, a set of additional peaks is observed in the low shift region when compared with the spectra of the 2H phase MoS<sub>2</sub> nanosheets in N–MoS<sub>2</sub> and N,Pt–MoS<sub>2</sub> nanosheets, identifiable as E<sub>1g</sub><sup>-</sup> (280 cm<sup>-1</sup>), J<sub>1</sub> (143 cm<sup>-1</sup>), J<sub>2</sub> (190 cm<sup>-1</sup>), and J<sub>3</sub> (334 cm<sup>-1</sup>) of the 1T phase MoS<sub>2</sub> (Fig. 7f). Furthermore, the N,Pt–MoS<sub>2</sub> nanosheets display very weak E<sub>12g</sub><sup>-</sup> and A<sub>1g</sub><sup>-</sup> signals, suggesting a high yield of the 1T phase. The XPS results (Fig. 7g) indicate that the phase compositions of the N–MoS<sub>2</sub> and N,Pt–MoS<sub>2</sub> nanosheets were 62% 1T and 38% 2H, and 87% 1T and 13% 2H, respectively; these results were obtained by analyzing the dominant peaks corresponding to the 2H and 1T phases.<sup>119</sup> Similarly, Pan *et al.* improved the catalytic properties of the MoS<sub>2</sub> nanostructures through phase engineering by boosting the edge density, activating the basal planes, increasing the interlayer spacing, and stabilizing the 1T phase.<sup>120</sup> The researchers produced 1T





**Fig. 7** (a) HRTEM images of N,Pt-MoS<sub>2</sub> nanosheets, (b) schematic illustration with (below) HRTEM image of the lattice structures of 2H and 1T phases of MoS<sub>2</sub> nanosheets, (c) atomic arrangement profiles along the marked lines in green areas show the 2H phase and other areas show the 1T phase, (d) Structural illustration of N,Pt-MoS<sub>2</sub> nanosheets, (e) X-ray diffraction (XRD) patterns, (f) Raman spectra, and (g) X-ray photoelectron spectroscopy (XPS) spectra of Mo 3d for MoS<sub>2</sub>, N-MoS<sub>2</sub>, and N,Pt-MoS<sub>2</sub> nanosheets. The green and pink areas show the contribution of the 2H and 1T phases to the Mo 3d peaks. Reprinted with permission.<sup>119</sup> Copyright 2022, Royal Society of Chemistry. (h) TEM images at higher magnification showing inter-layer spacing with distances of ~0.82 nm, High-resolution XPS spectra of (i) Mo 3d, and (j) S 2p for 1T-Ni<sub>0.2</sub>Mo<sub>0.8</sub>S<sub>1.8</sub>P<sub>0.2</sub>. Reprinted with permission.<sup>120</sup> Copyright 2020, Royal Society of Chemistry.

phase-rich MoS<sub>2</sub> by doping and intercalating Ni and P (Ni<sub>0.2</sub>Mo<sub>0.8</sub>S<sub>1.8</sub>P<sub>0.2</sub>) in a single-step hydrothermal process. Codoping with Ni and P enriches the 1T phase, increases the interlayer spacing by 24% (Fig. 7h), significantly activates the basal planes, and increases the edge density of the MoS<sub>2</sub> nanostructures. High-resolution XPS analysis of Mo 3d indicated peaks occurring at 231.5 eV (Mo 3d<sub>3/2</sub>) and 228.3 eV (Mo 3d<sub>5/2</sub>) linked to the 1T-phase, alongside peaks at 232.6 eV (Mo 3d<sub>3/2</sub>) and 229.3 eV (Mo 3d<sub>5/2</sub>) associated with the 2H-phase (Fig. 7i).<sup>120</sup> In both scenarios, the peak intensities for Mo 3d<sub>3/2</sub> and Mo 3d<sub>5/2</sub> of the 1T-phase are significantly greater than those of the 2H-phase, signifying an enrichment of the 1T-phase in Ni<sub>0.2</sub>Mo<sub>0.8</sub>S<sub>1.8</sub>P<sub>0.2</sub> within the 2D nanostructures. The S 2p XPS spectrum (Fig. 7j) contained peaks at 164.6 eV (S 2p<sub>3/2</sub>) and 161.9 eV (S 2p<sub>1/2</sub>) indicative of the 2H-phase, as well as peaks at 162.8 eV (S 2p<sub>3/2</sub>) and 161.1 eV (S 2p<sub>1/2</sub>) associated with the 1T-phase of Ni<sub>0.2</sub>Mo<sub>0.8</sub>S<sub>1.8</sub>P<sub>0.2</sub>.<sup>120</sup> In this instance, the intensity of the peaks for the 1T-phase is also significantly

greater than that of the 2H-phase, confirming the phase transition from 2H to 1T in Ni<sub>0.2</sub>Mo<sub>0.8</sub>S<sub>1.8</sub>P<sub>0.2</sub> nanostructures.

ReS<sub>2</sub> generally exists in the distorted-1T phase owing to the zigzag Re-Re bonding structure.<sup>121</sup> Re is becoming a viable dopant to induce phase transition because it has a different number of valence electrons and a similar radius to those of Mo. Therefore, Re-doping into 2H-MoS<sub>2</sub> can transform the phase into 1T or distorted 1T.<sup>122</sup> Yu *et al.* developed single-atomic-Re-assisted 2H-to-1T phase-engineered MoS<sub>2</sub> nanosheets to increase electrocatalytic hydrogen production.<sup>123</sup> Researchers have described a straightforward one-pot hydrothermal technique and Ar-calcination that uses Re-doping to alter the phase of MoS<sub>2</sub> nanosheets by over 85% (Fig. 8a). The XRD diffraction (Fig. 8b) results revealed that the (002) facets of Re-SA/MoS<sub>2</sub> shifted to lower 2θ values with Re ion addition, indicating successful doping into the MoS<sub>2</sub> lattice.<sup>123</sup> HR-TEM images (Fig. 8c and d) indicated that Re-SA/MoS<sub>2</sub> had a flower-like nanosheet structure, with a lattice fringe distance of 0.69 nm, slightly larger than that of





**Fig. 8** (a) Schematic illustration of the fabrication of the Re-SA/MoS<sub>2</sub> catalyst, (b) XRD patterns of the MoS<sub>2</sub> and Re-SA/MoS<sub>2</sub> catalysts, (c) and (d) TEM and HRTEM images of the Re-SA/MoS<sub>2</sub> catalyst, HER performances of the Re-SA/MoS<sub>2</sub> electrocatalysts and control samples in H<sub>2</sub>-saturated 1.0 M KOH: (e) LSV curves with (f) overpotentials at current densities of  $-10$  and  $-100$  mA cm<sup>-2</sup>, and the HER performances of Re-SA/MoS<sub>2</sub> electrocatalysts and control samples in H<sub>2</sub>-saturated 0.5 M H<sub>2</sub>SO<sub>4</sub>: (g) LSV curves with (h) overpotentials at current densities of  $-10$  and  $-100$  mA cm<sup>-2</sup>. Reprinted with permission.<sup>123</sup> Copyright 2023, Royal Society of Chemistry. (i) Schematic diagram of the atomic structure 1T-SnS<sub>2</sub>, 1T'-Sn<sub>0.3</sub>W<sub>0.7</sub>S<sub>2</sub>, and 2H-WS<sub>2</sub>. HER performance of 2D metallic Sn<sub>0.3</sub>W<sub>0.7</sub>S<sub>2</sub> + CB: (j) cathodic polarization curves of different catalysts, (k) corresponding Tafel slopes, (l) durability test by chronoamperometry curve of Sn<sub>0.3</sub>W<sub>0.7</sub>S<sub>2</sub> + CB at 10 mA cm<sup>-2</sup>, Inset: Low-magnification TEM morphology after 30 000 s. Reprinted with permission.<sup>124</sup> Copyright 2019, Wiley-VCH.

pristine MoS<sub>2</sub> (0.65 nm), which reflects lattice expansion, consistent with the XRD results.<sup>123</sup>

For the HER, the resultant single-atomic Re-doped 1T-2H MoS<sub>2</sub> heterostructures provided modest overpotentials of 38 and 34 mV in alkaline and acidic environments, (Fig. 8e–h) respectively, at a current density of 10 mA cm<sup>-2</sup>.<sup>123</sup> Implantation of the Re single-atom facilitates the phase transition of MoS<sub>2</sub> from the 2H to 1T phase and charge redistribution through the constructed Re–S–Mo site, and serves as the active site to aid in the dissociation of water and the adsorption of the hydrogen intermediate.

The 1T' phase structure improves the HER activity by enhancing electrical conductivity and promoting electron movement. SnS<sub>2</sub> typically displays a 1T phase, whereas WS<sub>2</sub> displays a 2H phase. Both the 1T and 2H phases are

thermodynamically stable; SnS<sub>2</sub> and WS<sub>2</sub> behave as semiconductors. Nonetheless, Shao *et al.* developed 2D Sn<sub>1-x</sub>W<sub>x</sub>S<sub>2</sub> alloys with varying  $x$  values by adjusting the molar ratios of the reactants *via* hydrothermal synthesis (Fig. 8i).<sup>124</sup> Among these alloys, Sn<sub>0.3</sub>W<sub>0.7</sub>S<sub>2</sub> displays the highest concentration of the metallic phase at 81% and is distinguished by a distorted octahedral-coordinated metastable (1T') phase structure. The linear polarization curves indicate that Sn<sub>0.3</sub>W<sub>0.7</sub>S<sub>2</sub> + CB has significantly enhanced catalytic performance for the HER, with a current density 215 times greater than that of pure SnS<sub>2</sub> at  $-0.350$  V (Fig. 8j).<sup>124</sup> In addition, Sn<sub>0.3</sub>W<sub>0.7</sub>S<sub>2</sub> displays a current density 13 times higher than that of pure SnS<sub>2</sub> at  $-0.550$  V, while Sn<sub>0.3</sub>W<sub>0.7</sub>S<sub>2</sub> + CB exhibits a current density 93 times higher than that of SnS<sub>2</sub> + CB at  $-0.350$  V (Fig. 8j). The metallic 1T'-Sn<sub>0.3</sub>W<sub>0.7</sub>S<sub>2</sub> exhibits high intrinsic conductivity and lattice



distortion, which contribute to its improved catalytic performance. The significantly lower Tafel value of  $1T'-\text{Sn}_{0.3}\text{W}_{0.7}\text{S}_2$  ( $114 \text{ mV dec}^{-1}$ ) compared with that of  $\text{SnS}_2$  ( $398 \text{ mV dec}^{-1}$ ) indicates enhanced catalytic performance due to W addition (Fig. 8k). The Tafel value of  $81 \text{ mV dec}^{-1}$  for  $\text{Sn}_{0.3}\text{W}_{0.7}\text{S}_2 + \text{CB}$  indicates that a mix of Volmer and Heyrovsky reactions occurs (Fig. 8k).<sup>124</sup> The reduced Tafel slope is associated with more active sites from crystal structure distortion and faster electron transfer at the solid-liquid interface. Additionally, the  $\text{Sn}_{0.3}\text{W}_{0.7}\text{S}_2 + \text{CB}$  nanohybrid electrode shows minimal decline in the cathodic current after 30 000 seconds (Fig. 8l), indicating strong electrochemical stability, while  $1T'-\text{Sn}_{0.3}\text{W}_{0.7}\text{S}_2$  maintains its morphology and structure (Fig. 8l, inset).<sup>124</sup> Additionally, Table 1 presents a summary of the literature on phase engineering involving electrocatalysts for the HER.

### 3.4. Interface tuning by alloying

The design of metal alloys represents a highly promising strategy for effectively customizing the properties of metal catalysts, thereby enhancing their performance in various catalytic processes.<sup>125</sup> One of the key advantages of utilizing poly-metallic materials lies in the unique interactions between different metal atoms at their interfaces. These interactions can lead to a significant increase in catalytic activity, driven by both geometric and electronic effects that result from the combination of multiple metals. Typically, alloys are characterized by specific scaling relationships that can influence their catalytic performance. However, the technique of microalloying could have the potential to induce phenomena such as band narrowing and unique adsorption characteristics that cannot be accurately predicted through traditional linear interpolation methods.<sup>126</sup> This is primarily due to the distinct bonding environment presented by isolated single-metal sites. For instance, surface alloys consisting of catalytically active single atoms such as Au, Pt, and Pd, anchored onto a more stable host surface have demonstrated remarkable performance across a range of catalytic applications.<sup>127</sup> This approach implies that no physical bonds are formed between the disparate active sites. Consequently, the intermetallic interactions occurring at the interfaces of the two metals differ fundamentally from those observed in conventional bulk alloys. Moreover, this single-site approach is particularly advantageous because it allows the atomic utilization rates to reach 100%. The high level of efficiency significantly lowers the costs associated with catalytic processes and addresses the growing concerns regarding the scarcity and sustainability of precious metals often required in catalytic applications. By optimizing the design of these alloys, researchers could fabricate more efficient catalytic systems, ultimately promoting advances in industrial and technological applications.

Alloying serves as an effective strategy to enhance the thermodynamic stability of metastable-phase materials by incorporating larger-radius atoms that help stabilize loosely arranged atoms. TMs have a wide variety of crystal phases; for instance, both fcc and bcc structures can be identified in iron, which increases the potential for creating metastable phase

transition metal alloys.<sup>128</sup> Moreover, introducing a small quantity of noble metals into a TM matrix can help maintain the TM atoms in the metastable state throughout the thermodynamic transformation process. Li *et al.* synthesized a nanoporous metastable fcc Fe-Pd alloy through electrochemical dealloying.<sup>129</sup> The precursor ribbon of the Fe-Pd alloy was fabricated using melt-spinning techniques (Fig. 9a). The nanoporous Fe-Pd alloys were subsequently produced *via* electrochemical dealloying, where the crystal structure of the nanoporous layer is adjusted by varying the applied potentials, which are linked to the differing electrochemical stabilities of the bcc and fcc phases.<sup>129</sup> At lower dealloying potentials, the more reactive bcc phase is selectively removed from the precursor alloy, resulting in the formation of the nanoporous fcc Fe-Pd alloy.<sup>129</sup> By contrast, at higher dealloying potentials, both the fcc and bcc phases dissolve simultaneously. The fcc phase leaches out completely because of its low concentration in the precursor alloy, whereas the bcc phase remains partially intact.

The diffraction peaks of both crystalline phases shift toward a lower angle compared with that of metallic bcc Fe, suggesting that the larger Pd atoms partially replace Fe atoms (Fig. 9b).<sup>129</sup> The presence of the metastable fcc phase is explained by the added Pd that restricts diffusion, thereby enabling the formation of a fcc phase across a wider range of compositions. Owing to alloying, the d-band center of the Pd active site moves away from the Fermi level, reducing the Pd-H interactions and lowering the energy threshold for water dissociation. As shown in Fig. 9c, the fcc Fe-Pd displays an overpotential of 58 mV at a current density of  $10 \text{ mA cm}^{-2}$ , which is less than that of bcc Fe (337 mV), bcc Fe-Pd (191 mV), commercial Pd/C catalyst (114 mV), and commercial Pt/C catalyst (70 mV).<sup>129</sup> Furthermore, the fcc Fe-Pd demonstrates lower HER overpotentials at elevated current densities, highlighting its potential for industrial applications.

Rapid Joule heating was identified by Zhao *et al.* as a viable approach for creating highly efficient alloy-based electrocatalysts.<sup>130</sup> The researchers introduced a rapid Joule heating technique to effectively integrate the RuMo alloy in the  $\text{MoO}_x$  matrix. The produced catalyst demonstrates remarkable stability (2000 hours at  $1000 \text{ mA cm}^{-2}$ ) accompanied by an extremely low overpotential (9 mV, 18 mV, and 15 mV in 1 M KOH, 1 M PBS, and 0.5 M  $\text{H}_2\text{SO}_4$  solutions, respectively) at a current density of  $10 \text{ mA cm}^{-2}$ .<sup>130</sup> The RuMo@ $\text{MoO}_x$ -JH displays superior mass-normalized activity compared with that of the Pt/C electrode ( $10.2 \text{ A mgRu}^{-1}$  vs.  $2.9 \text{ A mgPt}^{-1}$  at 200 mV) (Fig. 9d). The normalized activity, based on cost, was obtained by dividing the geometric current density by the respective cost of the Pt-group-materials (PGM) (Fig. 9d), by considering the prices of different metals.<sup>130</sup> As anticipated, the RuMo@ $\text{MoO}_x$ -JH catalyst greatly surpassed the Pt/C in this metric ( $1486.9 \text{ A dollarRu}^{-1}$  vs.  $84.4 \text{ A dollarPt}^{-1}$  at 200 mV), highlighting the advantage from a sustainability perspective. Furthermore, the electrochemical kinetics were assessed using electrochemical impedance spectroscopy (EIS) measurements (Fig. 9e), confirming the lowest charge transfer resistance ( $R_{ct}$ ) of RuMo@ $\text{MoO}_x$ -





**Fig. 9** (a) Preparation and characterization of nanoporous Fe–Pd ribbons with a schematic illustration of Fe-based nanopores comprising an adjustable phase formed through an electrochemical dealloying strategy, (b) XRD patterns of nanoporous Fe–Pd samples, (c) LSV curves for the HER electrocatalytic performance of nanoporous Fe–Pd alloys in 1 M KOH solution. Reprinted with permission.<sup>129</sup> Copyright 2024, Elsevier. (d) Mass activities and calculated price activities for RuMo@MoO<sub>x</sub>-JH and Pt/C, (e) Nyquist plots measured in 1 M KOH solution. Reprinted with permission.<sup>130</sup> Copyright 2024, Springer Nature. (f) Schematic illustration of the formation of nanoporous NiFeAl/NF electrode, (g) Brunauer–Emmett–Teller (BET) surface area and C<sub>dl</sub> value, (h) compressive strength of different electrocatalysts, and (f) Stability curves of the Ni<sub>18</sub>Fe<sub>12</sub>Al<sub>70</sub> electrode at current densities of 100 and 400 mA cm<sup>-2</sup> for 100 h. Reprinted with permission.<sup>131</sup> Copyright 2023, Wiley-VCH.

JH among that of all samples at an applied overpotential of –75 mV.

Liu *et al.* developed a self-supporting hybrid system that includes Ni<sub>2</sub>Al<sub>3</sub> and Ni<sub>3</sub>Fe phases by incorporating aluminum on NF using lasers.<sup>131</sup> High-energy ball milling was used to adequately mix the stoichiometric NiFeAl powders and accelerate the amorphization kinetics of the NiFeAl compounds (Fig. 9f). The NF was subsequently covered with NiFeAl powder to create a consistent and compact layer, which was scanned using a high-energy laser beam. Following laser treatment, the powders formed a metallurgical bond with the underlying material (Fig. 9f). Eventually, some of the aluminum present in the newly formed electrode was removed by etching in a KOH

solution, resulting in a nanoporous structure of NiFeAl.<sup>131</sup> Non-toxic aluminum is suitable for use in the dealloying process. Ni<sub>18</sub>Fe<sub>12</sub>Al<sub>70</sub> (comprising Ni<sub>2</sub>Al<sub>3</sub> and Ni<sub>3</sub>Fe) exhibits an exceptionally low overpotential, which is necessary for initiating the HER. The researchers analyzed the optimal proportions of Ni and Fe, noting that the poor performance of Ni<sub>30</sub>Fe<sub>20</sub>Al<sub>50</sub> stems from the elevated levels of inert Ni and Fe atoms. When the number of inert atoms surpasses a specific limit, the dealloying corrosion affects only a few atomic layers on the alloy surface, preventing the development of a porous structure across the entire alloy system. The BET surface areas were 3.75, 4.66, 6.16, and 8.78 m<sup>2</sup> g<sup>-1</sup> for the alloys Ni<sub>30</sub>Fe<sub>20</sub>Al<sub>50</sub>, Ni<sub>18</sub>Fe<sub>12</sub>Al<sub>70</sub>, Ni<sub>12</sub>Fe<sub>8</sub>Al<sub>80</sub>, and Ni<sub>6</sub>Fe<sub>4</sub>Al<sub>90</sub> respectively (Fig. 9g).<sup>131</sup> This



demonstrates that dealloying can create a nanoporous structure with a significant surface area, providing numerous active sites and efficient pathways for mass transfer, thereby enhancing the kinetics of the electrochemical reaction. The  $C_{dl}$  of  $Ni_{18}Fe_{12}Al_{70}$ ,  $Ni_{12}Fe_8Al_{80}$ , and  $Ni_6Fe_4Al_{90}$  electrodes were 35.43, 35.40, and 39.64  $mF\ cm^{-2}$ , that is, 1.7 times higher than that of  $Ni_{30}Fe_{20}Al_{50}$  under identical conditions (Fig. 9g).<sup>131</sup> The notable electrochemical surface area (ECSA) can also be linked to the porous channels formed through the dealloying process. A microcomputer-controlled electronic universal testing machine was used to characterize the compressive resistance of all the samples (Fig. 9h).  $Ni_{18}Fe_{12}Al_{70}$  exhibits optimal HER activity ( $\eta_{10} = 31\ mV$  and  $\eta_{100} = 188\ mV$ ) and a compressive strength of 1.74 MPa. Consequently, the long-term durability of  $Ni_{18}Fe_{12}Al_{70}$  was evaluated through chronopotentiometric measurements over one hundred hours in a 1.0 M KOH solution at current densities of 100 and 400  $mA\ cm^{-2}$ . The overpotential remained stable throughout the duration (Fig. 9i), confirming its exceptional stability, indicating that  $Ni_{18}Fe_{12}Al_{70}$  is a promising electrocatalyst for the HER.

### 3.5. Single-atom catalysts (SACs)

SACs are characterized by the presence of isolated metal atoms that are firmly anchored onto various support materials, rendering them particularly attractive for applications in the HER.<sup>132</sup> The unique structure of SACs allows for maximal utilization of metal atoms while benefiting from their distinctive catalytic properties, leading to greater efficiency in hydrogen production.<sup>133</sup> The formation of interfaces in SACs can alter their electronic structure and coordination, potentially reducing their catalytic activity for the HER. This is largely due to changes in charge distribution and metal-support interactions, as well as the risk of single atoms aggregating into clusters. However, optimizing interface engineering through precise synthesis and tailored support interactions can help maintain or enhance SACs' catalytic performance in HER.<sup>134–136</sup> The process of interface engineering focuses on optimizing the interactions between the isolated metal atoms, supporting substrate, and surrounding reaction environment. This involves a thorough examination of the electronic, geometric, and chemical properties of the interfaces. By manipulating these parameters, researchers aim to create a versatile and conducive environment that enhances the performance of the catalyst, allowing for improved reactivity and selectivity in HER processes.<sup>133</sup> Moreover, systematic design and optimization of these interfaces can lead to the development of highly efficient and stable SACs. Pt-based materials continue to be recognized as the most effective catalysts for the HER, primarily because of their superior ability to bind hydrogen atoms.<sup>137</sup> This optimal binding capability is crucial for facilitating the electrochemical reactions involved in hydrogen production.

However, the widespread adoption of Pt in large-scale electrolyzers for hydrogen generation has been significantly hindered by two main factors: its high cost and limited availability. These challenges limit many applications that aim to harness hydrogen as a clean energy source. To address this issue,

research has increasingly focused on the development of single-atom catalysts.<sup>138</sup> SACs can allow electrolyzers to retain the high intrinsic activity associated with Pt while considerably reducing the overall amount of Pt required. This approach enhances the economic viability of using Pt in hydrogen production and mitigates concerns related to resource scarcity, making SACs a promising approach for designing Pt-based electrocatalysts for HER applications. Jiang *et al.* reported the development of a single-atom Pt-decorated nanoporous  $Co_{0.85}Se$  (Pt/np- $Co_{0.85}Se$ ) through an electrochemically selective etching technique, demonstrating its effectiveness as an electrocatalyst for hydrogen evolution.<sup>139</sup> Drawing inspiration from the method of potential cycling for depositing Pt atoms on a working electrode, the processes of electrochemical vacancy generation and Pt-atom embedding were performed *via* cyclic voltammetry (CV) using Pt foil as a counter electrode in a three-electrode setup containing 0.5 M  $H_2SO_4$ .<sup>139</sup> Throughout the cyclic procedure, minor Co atoms were dissolved from the np- $Co_{0.85}Se$ , which led to the formation of Co vacancies, thereby creating anchor points for the incorporation of Pt atoms.

Core-level XPS analysis of the Pt 4f region for both Pt/C and Pt/np- $Co_{0.85}Se$  demonstrated distinct features (Fig. 10a). For Pt/C, the Pt 4f<sub>7/2</sub> and 4f<sub>5/2</sub> orbital peaks occurred at binding energies of 71.2 eV and 74.5 eV, respectively, providing clear evidence of the presence of metallic platinum (Pt<sup>0</sup>). By contrast, the Pt 4f orbitals of the Pt/np- $Co_{0.85}Se$  sample were shifted slightly; the peaks were observed at 71.8 eV and 75.1 eV. This shift suggests that the Pt atoms in this sample exhibit a partially positive charge (Pt<sup>δ+</sup>), which can be attributed to the electronic interactions occurring between the isolated Pt atoms and the np- $Co_{0.85}Se$  matrix. X-ray absorption spectroscopy (XAS) analysis helped elucidate the electronic and local structures of Pt/np- $Co_{0.85}Se$  catalysts.<sup>139</sup> The Pt L3-edge XANES (Fig. 10b) and FT-EXAFS (Fig. 10c) spectra are shown, alongside comparisons with Pt foil, commercial Pt/C, and PtO<sub>2</sub>.<sup>139</sup> The XANES spectra indicate that the white-line intensity of Pt/np- $Co_{0.85}Se$  is greater than that of both Pt foil and commercial Pt/C, suggesting a positive valence state (0.8, inset of Fig. 10b) for Pt atoms, which may be the result of electron transfer from Pt to Se in the Pt–Se bonds of Pt/np- $Co_{0.85}Se$ .<sup>139</sup> In XAS, X-rays interact with atoms, exciting electrons from core levels to higher energy states, resulting in sharp peaks known as “white lines” at the absorption edge of the spectrum which indicates the number of vacant electronic states. Thus, the white line is a key indicator of an atom's electronic structure and the availability of unoccupied states.<sup>140</sup> The FT-EXAFS spectra presented in Fig. 7c show a prominent peak at 2.03 Å corresponding to the Pt–Se contribution, which indicates the single-atom characteristic of Pt in Pt/np- $Co_{0.85}Se$ .

Despite notable advancements in Pt-supported atomic catalysts (Pt SACs), these methods continue to face challenges in effectively lowering the energy barrier associated with the dissociation of water during the Volmer step, which is the initial step of the overall electrochemical reaction. This high-energy barrier can hinder reaction kinetics, affecting the overall efficiency of processes such as hydrogen evolution.



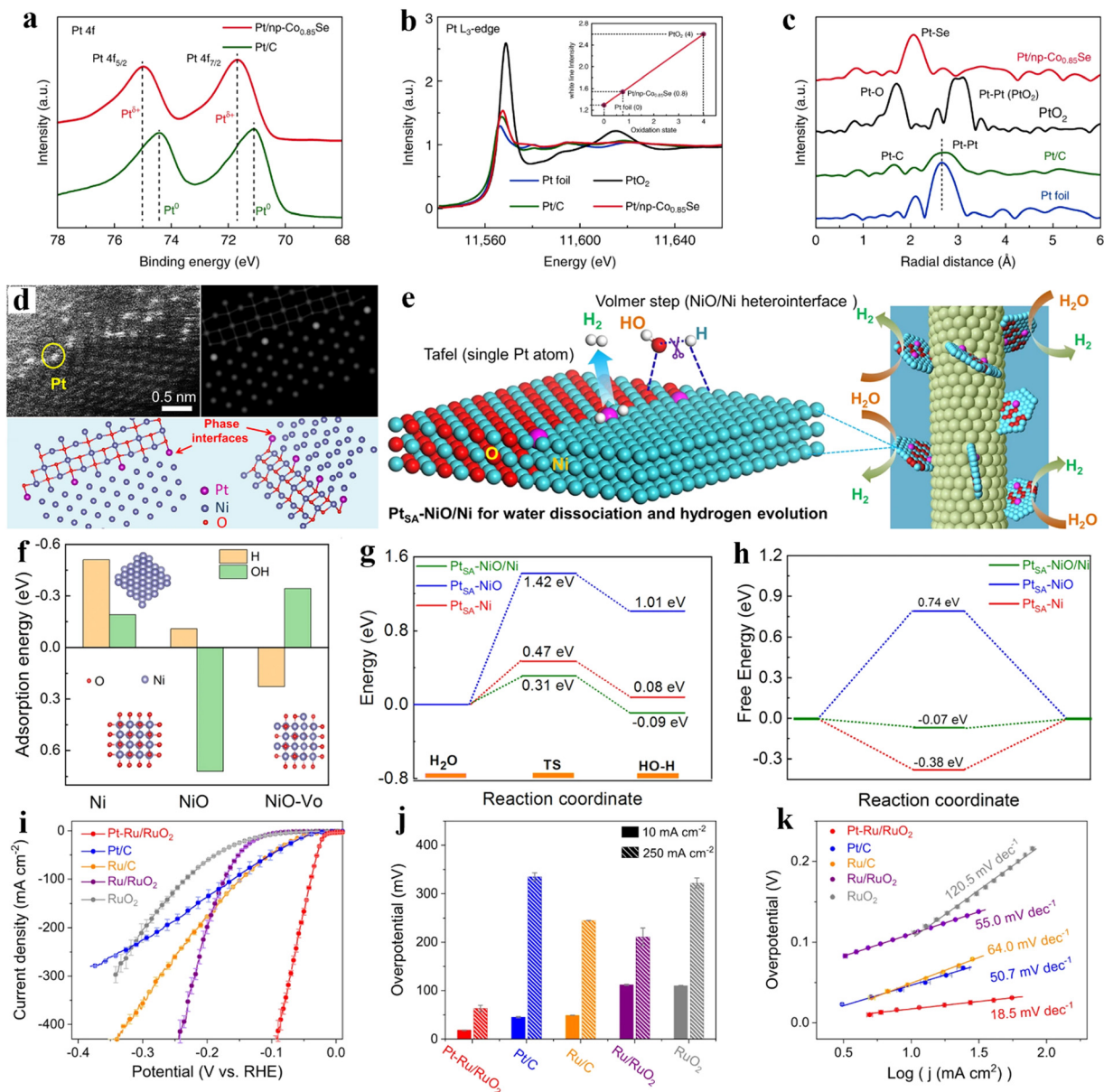


**Fig. 10** (a) XPS spectra of Pt/np-Co<sub>0.85</sub>Se and commercial Pt/C in Pt 4f regions, (b) normalized X-ray absorption near-edge structure (XANES) at the Pt L<sub>3</sub>-edge of Pt foil, commercial Pt/C, PtO<sub>2</sub>, and Pt/np-Co<sub>0.85</sub>Se (The inset shows the average oxidation state of Pt in Pt/np-Co<sub>0.85</sub>Se), (c) corresponding Fourier transform extended x-ray absorption fine structure (FT-EXAFS) spectra from (b). Reprinted with permission.<sup>139</sup> Copyright 2019, Springer Nature. (d) Magnified HAADF-STEM image of Pt<sub>tSA</sub>-NiO/Ni and the illustrated interface structure by DFT calculation, showing the atomically dispersed Pt atoms at Ni position (yellow color circle), (e) mechanism of Pt<sub>tSA</sub>-NiO/Ni network as an efficient catalyst toward large-scale water electrolysis in alkaline media, (f) calculated OH-binding energies ( $\Delta E_{OH}$ ) and H binding energies ( $\Delta E_H$ ) for Ni, pure NiO, and O vacancies-modified NiO surface, (g) calculated energy barriers of water dissociation kinetics, and (h) adsorption free energies of H\* on the surface of the Pt<sub>tSA</sub>-NiO/Ni, Pt<sub>tSA</sub>-NiO, and Pt<sub>tSA</sub>-Ni catalysts, respectively. Reprinted with permission.<sup>141</sup> Copyright 2021, Springer Nature. (i) Polarization curves with 95% iR corrections and (j) corresponding overpotentials of Pt-Ru/RuO<sub>2</sub>, Ru/RuO<sub>2</sub>, RuO<sub>2</sub>, Pt/C, and Ru/C at current densities of 10 mA cm<sup>-2</sup> and 250 mA cm<sup>-2</sup> in 1 M KOH, (k) Tafel plots derived from the polarization curves in (i). Reprinted with permission.<sup>142</sup> Copyright 2024, Springer Nature.

Typically, the dissociation of H<sub>2</sub>O and conversion of H\* occur at separate catalytic sites.<sup>8</sup> Particularly, the HER performance of Pt-based catalysts in alkaline environments is influenced by the efficacy of the binding of hydroxyl species (OH\*) to the catalyst. The kinetics of the HER in alkaline conditions can be fine-tuned by adjusting the binding energies of the reactants (OH and H\*) on dual active sites.<sup>143</sup> The energy barrier for water

dissociation in the Volmer step (step (i)) for Pt SACs in alkaline solutions might be lowered by incorporating or creating dual active sites in the catalyst, allowing for independent modulation of the binding energies of the reactants (OH\* and H\*).<sup>143</sup> Thus, Zhou *et al.* were inspired to design a two-dimensional metal/metal oxide heterostructure comprising nickel oxide (NiO) and Ni on a 1D conductive network of silver nanowires



(Ag NWs), which serves as a foundational support for Pt single-atom catalysts ( $\text{Pt}_{\text{SA}}$ ) on the NiO/Ni surface ( $\text{Pt}_{\text{SA}}\text{-NiO/Ni}$ ).<sup>141</sup> The design of the innovative heterostructure could boost the HER efficiency in alkaline conditions by taking advantage of the distinct characteristics of Pt single atoms distributed throughout the dual-phase support. The enlarged HAADF-STEM image (Fig. 10d) indicates that the single Pt atoms are primarily located at the interfaces of the NiO/Ni heterostructure.<sup>141</sup> The dissociation of water in the Volmer step under alkaline aqueous conditions is expected to be expedited by the O vacancy-modified NiO at the interfaces, which interacts strongly with OH. By contrast, metallic Ni interacts with H to destabilize the H–OH bond (step (i)) (Fig. 10e). In addition to the Volmer step, the single-atom Pt sites supported by the NiO/Ni heterostructure may have more favorable H binding properties for the conversion and release of dissociated H (step (ii)), thereby further enhancing the overall HER kinetics of  $\text{Pt}_{\text{SA}}\text{-NiO/Ni}$  in an alkaline environment.<sup>141</sup> DFT studies indicated that both H and OH exhibit weak binding to the pure NiO surface.

By contrast, the metallic Ni surface tends to stabilize H (Fig. 10f). Meanwhile, O-vacancy-modified NiO improves the adsorption of OH species (Fig. 10f). For the NiO/Ni composition, O vacancies at the NiO/Ni heterostructure interfaces arise from dislocations in the crystal lattice and phase transitions.<sup>141</sup> As a result, the NiO/Ni-coupled single-atom Pt catalyst displays the highest ability for  $\text{H}_2\text{O}$  adsorption and the most significant energy release of  $-0.09$  eV during the water dissociation that occurs in the Volmer step (Fig. 10g). Furthermore, the  $\text{Pt}_{\text{SA}}\text{-NiO/Ni}$  hybrid catalyst has a minimal energy barrier ( $0.31$  eV) to dissociate  $\text{H}_2\text{O}$  into  $\text{OH}^*$  and H with the aid of NiO/Ni interfaces. In the following step, the single-atom Pt sites supported at the NiO/Ni interfaces function as proton acceptors for the recombination of the dissociated protons ( $\text{H}^*$ ) and evolution of  $\text{H}_2$ , owing to their near-zero H binding energy ( $-0.07$  eV, Fig. 10h).<sup>141</sup> The dual-interface catalyst harnesses the synergistic effects between the metal and metal oxide components, optimizing the reaction pathways and enhancing the catalytic HER performance.

Similarly, Zhu *et al.* synthesized hetero-interfaced Ru/RuO<sub>2</sub> doped with Pt single atoms by submerging the  $\text{RuCl}_3$  precursor in molten  $\text{NaNO}_3$ .<sup>142</sup> Afterward, Pt species were incorporated into the synthesized RuO<sub>2</sub>, followed by calcination in an *arGOn* atmosphere, leading to the integration of single Pt atoms and a slight reduction of RuO<sub>2</sub> to create interfaced Ru/RuO<sub>2</sub>. The researchers suggested that RuO<sub>2</sub> enhances sluggish water dissociation, whereas both Pt single atoms and metallic Ru promote the subsequent combination of  $\text{H}^*$ .<sup>142</sup> As shown in Fig. 10i, the LSV curves with a 95% iR correction demonstrate the activity hierarchy of  $\text{Pt-Ru/RuO}_2 > \text{Pt/C} > \text{Ru/C} > \text{Ru/RuO}_2 > \text{RuO}_2$  at lower potentials. Specifically,  $\text{Pt-Ru/RuO}_2$  exhibits an overpotential of 18 mV at a current density of  $10 \text{ mA cm}^{-2}$  in 1 M KOH for the HER, which is significantly lower than those of Pt/C (45 mV), Ru/C (49 mV), Ru/RuO<sub>2</sub> (112 mV), and RuO<sub>2</sub> (110 mV) (Fig. 10j). Remarkably, at a higher current density of  $250 \text{ mA cm}^{-2}$ ,  $\text{Pt-Ru/RuO}_2$  maintains the lowest overpotential (63 mV) among those of all the

electrocatalysts assessed, indicating its exceptional alkaline HER performance. Additionally, Fig. 10k depicts the Tafel slopes derived from the LSV curves, with values of  $18.5 \text{ mV dec}^{-1}$ ,  $50.7 \text{ mV dec}^{-1}$ ,  $64.0 \text{ mV dec}^{-1}$ ,  $55.0 \text{ mV dec}^{-1}$ , and  $120.5 \text{ mV dec}^{-1}$  for  $\text{Pt-Ru/RuO}_2$ , Pt/C, Ru/C, Ru/RuO<sub>2</sub>, and RuO<sub>2</sub>, respectively.<sup>142</sup> The lowest Tafel slope observed in  $\text{Pt-Ru/RuO}_2$  signifies the most efficient facilitation of hydrogen evolution kinetics. Furthermore, the low Tafel slope associated with  $\text{Pt-Ru/RuO}_2$  suggests that it adheres to the Volmer–Tafel mechanism in the alkaline HER following the incorporation of Pt single atoms, which feature high hydrogen coverage and binding capacity.<sup>142</sup> SACs possess unique electronic characteristics resulting from their specific coordination environments, charge distribution, and quantum confinement phenomena. The individual metal atoms in SACs engage in strong interactions with the surrounding support, which leads to electronic states that are considerably different from those found in bulk materials.<sup>144</sup> This modified coordination environment causes a redistribution of charge, wherein the electron density shifts between the metal atom and the support, thus altering their catalytic performance. Additionally, the quantum confinement effects in SACs limit the electronic states of the metal atoms, which boosts their reactivity by adjusting the d-band center. Together, these elements significantly enhance the remarkable catalytic efficacy of SACs, rendering them exceptionally effective for electrocatalytic processes.

## 4. Challenges and future directions

The rapid advancement of clean energy technologies is fueled by growing concerns about environmental pollution and rising global energy demands. Hydrogen, a promising renewable energy source, is primarily generated through water electrolysis, which is considered a safe and viable approach for sustainable energy development. This method effectively utilizes renewable energy sources like solar, wind, and geothermal power, making it essential for a clean energy future. Recent developments in interface engineering of noble and non-noble-metal-based electrocatalysts for the HER in both alkaline and acidic environments have been discussed. While noble-metal catalysts are favored for their favorable energy characteristics, their instability poses challenges for long-term use, leading to increased research on enhancing their durability.

Interface engineering offers a suite of design strategies, such as the development of heterostructures, core-shell configurations, phase engineering, alloying, and the development of SACs, that can significantly affect electrocatalytic performance during the HER. Despite from becoming a key strategy for improving HER electrocatalysis, several fundamental challenges persist for interface engineering.

First, the exact role of interfacial electronic structures in influencing catalytic activity is not yet fully understood. Key factors such as charge redistribution, defect engineering, and modifications to the d-band center are critical for optimizing hydrogen adsorption, water dissociation, and charge



transfer. However, more research is needed to quantify their contributions. Second, the long-term stability of engineered interfaces poses a significant challenge. Many catalysts experience issues such as phase segregation, metal leaching, and collapse of the heterostructure under electrochemical conditions. To develop more durable materials, advanced operando techniques are necessary for real-time monitoring of interfacial changes.

Third, designing interfaces that achieve an optimal balance for hydrogen adsorption and desorption is still difficult. Techniques like strain engineering, heteroatomic doping, and charge-transfer modulation have shown promise in tuning the hydrogen adsorption free energy ( $\Delta G_{H^+}$ ), but further refinement is needed to ensure efficient HER kinetics. Fourth, challenges remain regarding the scalability and reproducibility of interface-modified catalysts. While many catalysts demonstrate excellent performance under controlled laboratory conditions, translating these materials into large-scale, cost-effective, and high-performance systems is still a significant hurdle.

Lastly, a key unresolved question is whether interfacial modifications can reliably maintain their catalytic benefits over extended operational lifetimes. Future research should prioritize stabilizing dynamic interfacial structures and using *in situ* and operando characterization techniques to monitor surface and compositional changes under real-world conditions. Addressing these challenges will deepen our understanding of interface effects and accelerate the development of next-generation HER catalysts for industrial use.

Key aspects, including modifications to the electronic structure, presence of synergistic effects, and optimization of the chemisorption of reaction intermediates, require further investigation. More thorough characterization must be performed of the reaction processes involved in electrocatalysis to clarify these interface effects and enhance the catalyst performance. Although the necessity for a more detailed characterization of reaction mechanisms in electrocatalysis to elucidate interface effects and improve catalyst performance has been highlighted, it is essential to acknowledge the considerable progress that has already been achieved in this field. Recent studies have made significant strides in analyzing the function of interfaces in electrocatalytic reactions. Scanning electrochemical microscopy (SECM) is an analytical method used to investigate surfaces from an electrochemical perspective and is recognized as a highly effective tool for obtaining electrochemical information. It features exceptional spatiotemporal resolution that allows for the visualization of localized electrochemical processes and surface characteristics.<sup>145</sup> X-ray absorption fine structure (SR-XAFS) and synchrotron Fourier-transform infrared spectroscopy (SR-FTIR) are discussed by Su *et al.*, that *in situ* SR-XAFS and SR-FTIR, particularly highlighting the multi-scale monitoring of the structural changes of active centers.<sup>146</sup> Furthermore, deeper mechanisms involved at the interfaces of electrocatalysts, emphasizing the significance of *in situ* electrochemical measurements to enhance the understanding and optimization of catalyst performance. Additionally,

electrochemical scanning probe microscopy (EC-SPM) has emerged as an essential experimental method because of its ability to capture surface topography with atomic-level resolution, even in the challenging conditions of electrolytes. As a result, EC-SPM techniques have significantly advanced our knowledge of electrocatalysis.<sup>147</sup> These investigations highlight the vital importance of interface engineering in boosting the efficiency and durability of electrocatalysts.

The practical applications of these catalysts, which necessitates the development of accessible and reliable synthetic methods, must be considered. These methods should focus on producing cost-efficient catalysts that feature high-quality interfaces and exhibit unique functionalities that improve their overall performance. Achieving this goal requires a deep understanding of the mechanisms governing the formation of high-quality interfaces in the catalysts. These insights could guide the design and synthesis of improved materials with tailored properties. Third, the role of reaction intermediates in influencing the electrocatalytic performance is another area that deserves deeper exploration. Current research on the impact of these intermediates on catalytic performance is limited. Therefore, detailed studies on the reaction intermediates of the model catalysts must be conducted using advanced *in situ* spectroscopic and microscopic techniques. These studies should aim to uncover the molecular-level mechanisms driving the electrocatalytic reactions, thus contributing to a more nuanced understanding of how these intermediates affect the overall catalytic activity. Fourth, integrating experimental findings with theoretical approaches is highly valuable for gaining insights into the fundamental origins of enhanced electrocatalytic activity. This dual strategy can be used to investigate the enhancements observed at atomic and molecular levels. By leveraging both computational models and practical experiments, researchers can develop effective strategies for designing high-performance electrocatalysts, specifically for the HER, thereby advancing the field of sustainable energy conversion. Finally, the unresolved question regarding whether the interface engineering of catalysts can consistently maintain their beneficial effects on the electrochemical properties over prolonged catalytic processes must be answered. To address this uncertainty, researchers should use a variety of techniques such as *in situ*, *ex situ*, and *operando* methods to accurately assess the surface compositions and structures of catalysts throughout their operational lifespan. This comprehensive analysis will help to determine the stability and effectiveness of interface modifications in catalytic applications.

## 5. Conclusion

The shift toward clean, renewable, and environmentally friendly energy sources, particularly those based on hydrogen, represents a crucial trend in the global pursuit of carbon neutrality. As various countries and organizations commit to reducing their carbon footprints, hydrogen energy is gaining significant attention for its potential to meet these



sustainability goals. Intensive research and development initiatives are currently underway to overcome the technological challenges associated with hydrogen production *via* water electrolysis. This process involves splitting water molecules into hydrogen and oxygen using electricity, which can be sourced from renewable energy technologies, such as solar, wind, or hydropower. As advances in materials science and electrochemical engineering continue, these innovations are expected to enhance the efficiency and cost-effectiveness of hydrogen production. In the near future, sustainable hydrogen energy will play a pivotal role in powering various applications ranging from industrial machinery to public transportation systems, subsequently improving the quality of life of individuals by providing cleaner energy alternatives. Water electrolysis is likely to emerge as the predominant method of hydrogen production, contributing significantly to the establishment of a hydrogen economy that fosters environmental sustainability and reduces reliance on fossil fuels.

We summarized the fundamental and experimental advances in tuning noble-metal- and non-noble-metal-based catalyst surfaces and interfaces to enhance HER electrocatalysis. Interfacial engineering of the catalysts endows them with increased active areas, strong synergistic effects, modified electronic structures, and facilitates adsorption energy, which enables them to display exceptional electrocatalytic performances. Additionally, facile strategies for the interface engineering of catalysts could also serve as a useful guide for the design and fabrication of catalytic structures with promising performances. Based on these advances, much progress has been made in the advanced electrocatalysis of catalysts through interface engineering. In this review, we provide a comprehensive overview of both the fundamental principles and experimental advances concerning the tuning of catalyst interfaces, specifically focusing on noble and non-noble-metal-based catalysts aimed at enhancing the electrocatalytic performance in the HER. Engineering of catalyst interfaces has proven to be a pivotal factor in increasing the active surface area, which directly contributes to improved catalytic activity. By optimizing these interfaces, researchers have achieved a strong synergistic effect among the different catalyst components, which is essential for promoting chemical reactions. Furthermore, interface engineering allows the modification of the electronic structure of catalysts, bolstering their effectiveness in facilitating reactions. This manipulation of the electronic properties also aids in adjusting the adsorption energies of the reactants on the catalyst surfaces, ensuring that the energy barriers for the reactions are lowered. Thus, the catalysts exhibit remarkable electrocatalytic performances. In addition to the enhanced performance, we highlighted the simple yet effective strategies for interface engineering that have emerged. These approaches provide valuable insights and guidelines for the rational design and fabrication of catalytic structures that exhibit superior performances. Overall, this review emphasizes the noteworthy progress and achievements in the field of advanced electrocatalysis through the innovative application of interface engineering. The findings discussed illustrate advances in catalyst

performance and underscore the potential for future research and development in this critical area of energy conversion technology.

## Data availability

No primary research results, software, or code have been included and no new data were generated or analyzed as part of this review.

## Conflicts of interest

The authors declare no conflict of interest.

## Acknowledgements

This research was supported by a National Research Foundation of Korea grant (RS-2024-00339674) funded by the Ministry of Science and ICT, Republic of Korea; the Technology Innovation Program (RS-2024-00424104 and RS-2024-00432811) funded by the Ministry of Trade, Industry & Energy (MOTIE, Korea); and the GRRC program of Gyeonggi Province (GRRC Hanyang 2020-B03).

## References

- 1 S. Chu and A. Majumdar, *Nature*, 2012, **488**, 294–303.
- 2 R. B. Ghising, U. N. Pan, D. R. Paudel, M. R. Kandel, N. H. Kim and J. H. Lee, *J. Mater. Chem. A*, 2022, **10**, 16457–16467.
- 3 S. Thompson, *Energies*, 2023, **16**, 6183.
- 4 B. Ye, B. Jeong, M.-J. Lee, T. H. Kim, S.-S. Park, J. Jung, S. Lee and H.-D. Kim, *Nano Convergence*, 2022, **9**, 51.
- 5 S. Küfeoğlu, in *Emerging Technologies: Value Creation for Sustainable Development*, ed. S. Küfeoğlu, Springer International Publishing, Cham, 2022, pp. 305–330.
- 6 D. Gielen, F. Boshell, D. Saygin, M. D. Bazilian, N. Wagner and R. Gorini, *Energy Strategy Rev.*, 2019, **24**, 38–50.
- 7 Q. P. Ngo, T. T. Nguyen, M. Singh, N. H. Kim and J. H. Lee, *J. Mater. Chem. A*, 2024, **12**, 1185–1199.
- 8 Q. P. Ngo, T. T. Nguyen, M. Singh, R. Balaji, N. H. Kim and J. H. Lee, *Appl. Catal., B*, 2023, **331**, 122674.
- 9 Z. Abdin, A. Zafaranloo, A. Rafiee, W. Mérida, W. Lipiński and K. R. Khalilpour, *Renewable Sustainable Energy Rev.*, 2020, **120**, 109620.
- 10 T. I. Singh, S. Li, G. Leem and S. Lee, *Photocatalytic Hydrogen Production for Sustainable Energy*, 2023, pp. 191–217.
- 11 Í. Martín-García, E. Rosales-Asensio, A. González-Martínez, S. Bracco, F. Delfino and M. de Simón-Martín, *Energy Rep.*, 2020, **6**, 155–166.
- 12 S. Singh, S. Jain, V. Ps, A. K. Tiwari, M. R. Nouni, J. K. Pandey and S. Goel, *Renewable Sustainable Energy Rev.*, 2015, **51**, 623–633.



- 13 P. P. Dhakal, U. N. Pan, D. R. Paudel, M. R. Kandel, N. H. Kim and J. H. Lee, *Mater. Today Nano*, 2022, **20**, 100272.
- 14 M. Singh, D. C. Cha, H. Kim, J. Park, S. Kim, C. G. Yoo, G. Leem and S. Lee, *Towards Sustainable and Green Hydrogen Production by Photocatalysis: Insights into Design and Development of Efficient Materials (Volume 2)*, American Chemical Society, 2024, vol. 1468, ch. 3, pp. 47–78.
- 15 M. R. Kandel, U. N. Pan, P. P. Dhakal, R. B. Ghising, S. Sidra, D. H. Kim, N. H. Kim and J. H. Lee, *Small*, 2024, **20**, 2307241.
- 16 B. Xiong, L. Chen and J. Shi, *ACS Catal.*, 2018, **8**, 3688–3707.
- 17 A. M. Appel and M. L. Helm, *ACS Catal.*, 2014, **4**, 630–633.
- 18 C. Feng, M. Chen, Z. Yang, Z. Xie, X. Li, S. Li, A. Abudula and G. Guan, *J. Mater. Sci. Technol.*, 2023, **162**, 203–226.
- 19 C. Das, N. Sinha and P. Roy, *Small*, 2022, **18**, 2202033.
- 20 S. H. Park, T. H. Jo, M. H. Lee, K. Kawashima, C. B. Mullins, H.-K. Lim and D. H. Youn, *J. Mater. Chem. A*, 2021, **9**, 4945–4951.
- 21 M. Shalom, D. Rössnig, X. Yang, G. Clavel, T. P. Fellinger and M. Antonietti, *J. Mater. Chem. A*, 2015, **3**, 8171–8177.
- 22 Y. P. Zhu, C. Guo, Y. Zheng and S.-Z. Qiao, *Acc. Chem. Res.*, 2017, **50**, 915–923.
- 23 Y. Zhang, Y. Lin, T. Duan and L. Song, *Mater. Today*, 2021, **48**, 115–134.
- 24 J. A. Raiford, S. T. Oyakhire and S. F. Bent, *Energy Environ. Sci.*, 2020, **13**, 1997–2023.
- 25 A. Falch, V. A. Lates, H. S. Kotzé and R. J. Kriek, *Electrocatalysis*, 2016, **7**, 33–41.
- 26 D. C. Cha, T. I. Singh, A. Maibam, T. H. Kim, D. H. Nam, R. Babarao and S. Lee, *Small*, 2023, **19**, 2301405.
- 27 K. S. Novoselov, A. Mishchenko, A. Carvalho and A. H. Castro Neto, *Science*, 2016, **353**, aac9439.
- 28 N. Choudhary, C. Li, H.-S. Chung, J. Moore, J. Thomas and Y. Jung, *ACS Nano*, 2016, **10**, 10726–10735.
- 29 D. Kim, J. Pandey, J. Jeong, W. Cho, S. Lee, S. Cho and H. Yang, *Chem. Rev.*, 2023, **123**, 11230–11268.
- 30 Y. Huang, S.-H. Wang, X. Wang, N. Omidvar, L. E. K. Achenie, S. E. Skrabalak and H. Xin, *J. Phys. Chem. C*, 2024, **128**, 11183–11189.
- 31 L. Kuai, Z. Chen, S. Liu, E. Kan, N. Yu, Y. Ren, C. Fang, X. Li, Y. Li and B. Geng, *Nat. Commun.*, 2020, **11**, 48.
- 32 M. Singh, D. C. Cha, T. I. Singh, A. Maibam, D. R. Paudel, D. H. Nam, T. H. Kim, S. Yoo and S. Lee, *Mater. Chem. Front.*, 2023, **7**, 6254–6280.
- 33 F. Lin, Z. Dong, Y. Yao, L. Yang, F. Fang and L. Jiao, *Adv. Energy Mater.*, 2020, **10**, 2002176.
- 34 C. Gao, F. Lyu and Y. Yin, *Chem. Rev.*, 2021, **121**, 834–881.
- 35 V.-H. Do and J.-M. Lee, *Chem. Soc. Rev.*, 2024, **53**, 2693–2737.
- 36 Z. Jin, L. Wang, T. Chen, J. Liang, Q. Zhang, W. Peng, Y. Li, F. Zhang and X. Fan, *Ind. Eng. Chem. Res.*, 2021, **60**, 5145–5150.
- 37 X. Li, W. Liu, M. Zhang, Y. Zhong, Z. Weng, Y. Mi, Y. Zhou, M. Li, J. J. Cha, Z. Tang, H. Jiang, X. Li and H. Wang, *Nano Lett.*, 2017, **17**, 2057–2063.
- 38 S. Shen, Z. Wang, Z. Lin, K. Song, Q. Zhang, F. Meng, L. Gu and W. Zhong, *Adv. Mater.*, 2022, **34**, 2110631.
- 39 H. Yen, Y. Seo, S. Kaliaguine and F. Kleitz, *ACS Catal.*, 2015, **5**, 5505–5511.
- 40 T. I. Singh, A. Maibam, D. C. Cha, S. Yoo, R. Babarao, S. U. Lee and S. Lee, *Adv. Sci.*, 2022, **9**, 2201311.
- 41 E. Marquis, F. Benini, B. Anasori, A. Rosenkranz and M. C. Righi, *Nano Convergence*, 2023, **10**, 16.
- 42 W. Li, G. Cheng, S. Peng, M. Sun, S. Wang, S. Han, Y. Liu, T. Zhai and L. Yu, *Chem. Eng. J.*, 2022, **430**, 132699.
- 43 Y. Zhu, Q. Lin, Y. Zhong, H. A. Tahini, Z. Shao and H. Wang, *Energy Environ. Sci.*, 2020, **13**, 3361–3392.
- 44 M. Singh, T. T. Nguyen, J. Balamurugan, N. H. Kim and J. H. Lee, *Chem. Eng. J.*, 2022, **430**, 132888.
- 45 H. Su, X. Pan, S. Li, H. Zhang and R. Zou, *Carbon Energy*, 2023, **5**, e296.
- 46 Q. Gao, W. Zhang, Z. Shi, L. Yang and Y. Tang, *Adv. Mater.*, 2019, **31**, 1802880.
- 47 J. Wu, T. Chen, C. Zhu, J. Du, L. Huang, J. Yan, D. Cai, C. Guan and C. Pan, *ACS Sustainable Chem. Eng.*, 2020, **8**, 4474–4480.
- 48 X. Xu, W. Xu, L. Zhang, G. Liu, X. Wang, W. Zhong and Y. Du, *Sep. Purif. Technol.*, 2021, **278**, 119569.
- 49 C.-J. Chen, P.-T. Chen, M. Basu, K.-C. Yang, Y.-R. Lu, C.-L. Dong, C.-G. Ma, C.-C. Shen, S.-F. Hu and R.-S. Liu, *J. Mater. Chem. A*, 2015, **3**, 23466–23476.
- 50 M. Jeon, H. Kim, S. Yoo, S. Park, G. Leem, S. Lee and J. H. Bang, *J. Ind. Eng. Chem.*, 2024, **140**, 190–195.
- 51 M. Bärtsch and M. Niederberger, *ChemPlusChem*, 2017, **82**, 42–59.
- 52 T. Hyeon Kim, S. Yoo, W. Kim, E. Jeong, G. Leem, S. Won Hong and S. Lee, *Appl. Surf. Sci.*, 2024, **672**, 160823.
- 53 J. Liu, X. Yang, F. Si, B. Zhao, X. Xi, L. Wang, J. Zhang, X.-Z. Fu and J.-L. Luo, *Nano Energy*, 2022, **103**, 107753.
- 54 G. Maduraiveeran, M. Sasidharan and W. Jin, *Prog. Mater. Sci.*, 2019, **106**, 100574.
- 55 B. You and S. Z. Qiao, *Chem. – Eur. J.*, 2021, **27**, 553–564.
- 56 H. H. Do, M. A. Tekalgne, Q. V. Le, J. H. Cho, S. H. Ahn and S. Y. Kim, *Nano Convergence*, 2023, **10**, 6.
- 57 S. Natarajan, M. Ulaganathan and V. Aravindan, *J. Mater. Chem. A*, 2021, **9**, 15542–15585.
- 58 W. Guo, J. Kim, H. Kim, S. Hong, H. Kim, S. Y. Kim and S. H. Ahn, *Mater. Today Chem.*, 2022, **24**, 100994.
- 59 Y. Tang, L. Dong, H. B. Wu and X.-Y. Yu, *J. Mater. Chem. A*, 2021, **9**, 1456–1462.
- 60 Y. Zhou, Y. Liu, H. Tang and B.-L. Lin, *J. Mater. Chem. A*, 2023, **11**, 10720–10726.
- 61 Q.-Q. Chen, X. Yang, C.-C. Hou, K. Li and Y. Chen, *J. Mater. Chem. A*, 2019, **7**, 11062–11068.
- 62 J. Li, W. Hong, C. Jian, Q. Cai and W. Liu, *Appl. Catal., B*, 2019, **244**, 320–326.
- 63 S. Li, W. Zang, X. Liu, S. J. Pennycook, Z. Kou, C. Yang, C. Guan and J. Wang, *Chem. Eng. J.*, 2019, **359**, 1419–1426.



- 64 L. Sun, H. Xu, Z. Cheng, D. Zheng, Q. Zhou, S. Yang and J. Lin, *Chem. Eng. J.*, 2022, **443**, 136348.
- 65 X. Han, N. Li, Y. B. Kang, Q. Dou, P. Xiong, Q. Liu, J. Y. Lee, L. Dai and H. S. Park, *ACS Energy Lett.*, 2021, **6**, 2460–2468.
- 66 L. Jiang, R. Wang, Z. Xiang and X. Wang, *Int. J. Hydrogen Energy*, 2024, **51**, 898–906.
- 67 M. Yao, B. Wang, B. Sun, L. Luo, Y. Chen, J. Wang, N. Wang, S. Komarneni, X. Niu and W. Hu, *Appl. Catal., B*, 2021, **280**, 119451.
- 68 Y. Qu, H. Medina, S.-W. Wang, Y.-C. Wang, C.-W. Chen, T.-Y. Su, A. Manikandan, K. Wang, Y.-C. Shih, J.-W. Chang, H.-C. Kuo, C.-Y. Lee, S.-Y. Lu, G. Shen, Z. M. Wang and Y.-L. Chueh, *Adv. Mater.*, 2016, **28**, 9831–9838.
- 69 T. An, Y. Wang, J. Tang, W. Wei, X. Cui, A. M. Alenizi, L. Zhang and G. Zheng, *J. Mater. Chem. A*, 2016, **4**, 13439–13443.
- 70 E. Son, S. Lee, J. Seo, U. Kim, S. H. Kim, J. M. Baik, Y.-K. Han and H. Park, *ACS Nano*, 2023, **17**, 10817–10826.
- 71 F. O.-T. Agyapong-Fordjour, S. J. Yun, H.-J. Kim, W. Choi, B. Kirubasankar, S. H. Choi, L. A. Adofo, S. Boandoh, Y. I. Kim, S. M. Kim, Y.-M. Kim, Y. H. Lee, Y.-K. Han and K. K. Kim, *Adv. Sci.*, 2021, **8**, 2003709.
- 72 C. C. Gudal, U. N. Pan, D. R. Paudel, M. R. Kandel, N. H. Kim and J. H. Lee, *ACS Appl. Mater. Interfaces*, 2022, **14**, 14492–14503.
- 73 M. Velpandian, A. Ragunathan, G. Ummethala, S. R. Krishna Malladi and P. Meduri, *ACS Appl. Energy Mater.*, 2023, **6**, 5968–5978.
- 74 D. Jiang, S. Xu, M. Gao, Y. Lu, Y. Liu, S. Sun and D. Li, *Inorg. Chem.*, 2021, **60**, 8189–8199.
- 75 I. H. Kwak, J. Y. Kim, G. M. Zewdie, J. Yang, K.-S. Lee, S. J. Yoo, I. S. Kwon, J. Park and H. S. Kang, *Adv. Mater.*, 2024, **36**, 2310769.
- 76 N. Khodayar, A. Noori, M. S. Rahmanifar, M. Moloudi, N. Hassani, M. Neek-Amal, M. F. El-Kady, N. B. Mohamed, X. Xia, Y. Zhang, R. B. Kaner and M. F. Mousavi, *Energy Environ. Sci.*, 2024, **17**, 5200–5215.
- 77 B. Guo, J. Zhao, Y. Xu, X. Wen, X. Ren, X. Huang, S. Niu, Y. Dai, R. Gao, P. Xu and S. Li, *ACS Appl. Mater. Interfaces*, 2024, **16**, 8939–8948.
- 78 L. Yan, B. Zhang, S. Wu and J. Yu, *J. Mater. Chem. A*, 2020, **8**, 14234–14242.
- 79 M. Yang, Y. Jiang, M. Qu, Y. Qin, Y. Wang, W. Shen, R. He, W. Su and M. Li, *Appl. Catal., B*, 2020, **269**, 118803.
- 80 H. Jin, Q. Gu, B. Chen, C. Tang, Y. Zheng, H. Zhang, M. Jaroniec and S.-Z. Qiao, *Chem*, 2020, **6**, 2382–2394.
- 81 Q. Qian, J. Zhang, J. Li, Y. Li, X. Jin, Y. Zhu, Y. Liu, Z. Li, A. El-Harairy, C. Xiao, G. Zhang and Y. Xie, *Angew. Chem., Int. Ed.*, 2021, **60**, 5984–5993.
- 82 Y. Lu, Z. Li, Y. Xu, L. Tang, S. Xu, D. Li, J. Zhu and D. Jiang, *Chem. Eng. J.*, 2021, **411**, 128433.
- 83 X. Zhou, Y. Mo, F. Yu, L. Liao, X. Yong, F. Zhang, D. Li, Q. Zhou, T. Sheng and H. Zhou, *Adv. Funct. Mater.*, 2023, **33**, 2209465.
- 84 H. Guo, A. Wu, Y. Xie, H. Yan, D. Wang, L. Wang and C. Tian, *J. Mater. Chem. A*, 2021, **9**, 8620–8629.
- 85 J. Chen, B. Ren, H. Cui and C. Wang, *Small*, 2020, **16**, 1907556.
- 86 V. H. Hoa, S. Prabhakaran, K. T. Nhi Le and D. H. Kim, *J. Mater. Chem. A*, 2022, **10**, 14604–14612.
- 87 W. Chen, B. Wu, Y. Wang, W. Zhou, Y. Li, T. Liu, C. Xie, L. Xu, S. Du, M. Song, D. Wang, Y. Liu, Y. Li, J. Liu, Y. Zou, R. Chen, C. Chen, J. Zheng, Y. Li, J. Chen and S. Wang, *Energy Environ. Sci.*, 2021, **14**, 6428–6440.
- 88 S. Ye, F. Luo, Q. Zhang, P. Zhang, T. Xu, Q. Wang, D. He, L. Guo, Y. Zhang, C. He, X. Ouyang, M. Gu, J. Liu and X. Sun, *Energy Environ. Sci.*, 2019, **12**, 1000–1007.
- 89 A. Shankar, S. Marimuthu and G. Maduraiveeran, *J. Mater. Chem. A*, 2024, **12**, 121–127.
- 90 J. Wei, K. Xiao, Y. Chen, X.-P. Guo, B. Huang and Z.-Q. Liu, *Energy Environ. Sci.*, 2022, **15**, 4592–4600.
- 91 W. Li, D. Yin, P. Li, X. Zhao and S. Hao, *Phys. Chem. Chem. Phys.*, 2024, **26**, 19822–19830.
- 92 M. Wu, R. Zhang, C. Li, X. Sun, G. Chen, L. Guo, K. Zheng and X. Sun, *Mater. Chem. Front.*, 2023, **7**, 4918–4927.
- 93 M. Luo, J. Cai, J. Zou, Z. Jiang, G. Wang and X. Kang, *J. Mater. Chem. A*, 2021, **9**, 14941–14947.
- 94 S. Ye, W. Xiong, P. Liao, L. Zheng, X. Ren, C. He, Q. Zhang and J. Liu, *J. Mater. Chem. A*, 2020, **8**, 11246–11254.
- 95 M. Yang, J. Wang, P. Dai, X. Tang, G. Li and L. Yang, *New J. Chem.*, 2024, **48**, 3942–3951.
- 96 Q. He, D. Tian, H. Jiang, D. Cao, S. Wei, D. Liu, P. Song, Y. Lin and L. Song, *Adv. Mater.*, 2020, **32**, 1906972.
- 97 J. Yang, W.-H. Li, S. Tan, K. Xu, Y. Wang, D. Wang and Y. Li, *Angew. Chem., Int. Ed.*, 2021, **60**, 19085–19091.
- 98 A. Kumar, V. Q. Bui, J. Lee, L. Wang, A. R. Jadhav, X. Liu, X. Shao, Y. Liu, J. Yu, Y. Hwang, H. T. D. Bui, S. Ajmal, M. G. Kim, S.-G. Kim, G.-S. Park, Y. Kawazoe and H. Lee, *Nat. Commun.*, 2021, **12**, 6766.
- 99 J. Wang, W. Fang, Y. Hu, Y. Zhang, J. Dang, Y. Wu, B. Chen, H. Zhao and Z. Li, *Appl. Catal., B*, 2021, **298**, 120490.
- 100 J. Zhu, L. Cai, X. Yin, Z. Wang, L. Zhang, H. Ma, Y. Ke, Y. Du, S. Xi, A. T. S. Wee, Y. Chai and W. Zhang, *ACS Nano*, 2020, **14**, 5600–5608.
- 101 X. Hu, J. Fan, R. Wang, M. Li, S. Sun, C. Xu and F. Pan, *Green Energy Environ.*, 2023, **8**, 601–611.
- 102 C. Y. Lee, T. H. Kim, J. Park, W. S. Yang and S. Lee, *Mater. Today Chem.*, 2024, **42**, 102433.
- 103 K. Mondal and A. Sharma, *RSC Adv.*, 2016, **6**, 83589–83612.
- 104 C. Yang, H. Lei, W. Z. Zhou, J. R. Zeng, Q. B. Zhang, Y. X. Hua and C. Y. Xu, *J. Mater. Chem. A*, 2018, **6**, 14281–14290.
- 105 Y. Li, Q. Zhang, L. Ren, Z. Li, X. Lin, Z. Ma, H. Yang, Z. Hu and J. Zou, *Ind. Chem. Mater.*, 2023, **1**, 282–298.
- 106 L. Yu, H. Zhou, J. Sun, F. Qin, D. Luo, L. Xie, F. Yu, J. Bao, Y. Li, Y. Yu, S. Chen and Z. Ren, *Nano Energy*, 2017, **41**, 327–336.
- 107 J. Ding, X. Jiang, C. Wang, Z. Zhu, C. Xu, Y. Zhou, X. Wang, Q. Liu, Z. Liu, Y. Tang, J. Lin and G. Fu, *J. Energy Chem.*, 2023, **86**, 510–517.
- 108 K. Kusada, H. Kobayashi, T. Yamamoto, S. Matsumura, N. Sumi, K. Sato, K. Nagaoka, Y. Kubota and H. Kitagawa, *J. Am. Chem. Soc.*, 2013, **135**, 5493–5496.



- 109 S. Han, Q. Yun, S. Tu, L. Zhu, W. Cao and Q. Lu, *J. Mater. Chem. A*, 2019, **7**, 24691–24714.
- 110 R. Ma, Y. Wang, G. Li, L. Yang, S. Liu, Z. Jin, X. Zhao, J. Ge and W. Xing, *Nano Res.*, 2021, **14**, 4321–4327.
- 111 C. Wang, Y. Li, C. Gu, L. Zhang, X. Wang and J. Tu, *Chem. Eng. J.*, 2022, **429**, 132226.
- 112 W. Yuan, T. Jiang, X. Fang, Y. Fan, S. Qian, Y. Gao, N. Cheng, H. Xue and J. Tian, *Chem. Eng. J.*, 2022, **439**, 135743.
- 113 Y. Q. Cheng and E. Ma, *Prog. Mater. Sci.*, 2011, **56**, 379–473.
- 114 M. Singh, T. T. Nguyen, P. Muthu Austeria, Q. P. Ngo, D. H. Kim, N. H. Kim and J. H. Lee, *Small*, 2023, **19**, 2206726.
- 115 U. N. Pan, V. Sharma, T. Kshetri, T. I. Singh, D. R. Paudel, N. H. Kim and J. H. Lee, *Small*, 2020, **16**, 2001691.
- 116 U. Gupta and C. N. R. Rao, *Nano Energy*, 2017, **41**, 49–65.
- 117 H. Wei, A. Tan, W. Liu, J. Piao, K. Wan, Z. Liang, Z. Xiang and Z. Fu, *Catalysts*, 2022, **12**, 947.
- 118 P. Chang, T. Wang, Z. Liu, X. Wang, J. Zhang, H. Xiao, L. Guan and J. Tao, *J. Mater. Chem. A*, 2022, **10**, 16115–16126.
- 119 Y. Sun, Y. Zang, W. Tian, X. Yu, J. Qi, L. Chen, X. Liu and H. Qiu, *Energy Environ. Sci.*, 2022, **15**, 1201–1210.
- 120 U. N. Pan, T. I. Singh, D. R. Paudel, C. C. Gudal, N. H. Kim and J. H. Lee, *J. Mater. Chem. A*, 2020, **8**, 19654–19664.
- 121 Q. Pang, X. Fan, K. Sun, K. Xiang, L. Dong, S. Zhao, Y. D. Kim, B. Li, Q. Liu, Z. Liu and Z. Peng, *J. Mater. Chem. A*, 2023, **11**, 14451–14468.
- 122 X. Tian, D. S. Kim, S. Yang, C. J. Ciccarino, Y. Gong, Y. Yang, Y. Yang, B. Duschatko, Y. Yuan, P. M. Ajayan, J. C. Idrobo, P. Narang and J. Miao, *Nat. Mater.*, 2020, **19**, 867–873.
- 123 J. Yu, Y. Qian, Q. Wang, C. Su, H. Lee, L. Shang and T. Zhang, *EES Catal.*, 2023, **1**, 571–579.
- 124 G. Shao, X.-X. Xue, B. Wu, Y.-C. Lin, M. Ouzounian, T. S. Hu, Y. Xu, X. Liu, S. Li, K. Suenaga, Y. Feng and S. Liu, *Adv. Funct. Mater.*, 2020, **30**, 1906069.
- 125 W. Ren, X. Tan, J. Qu, S. Li, J. Li, X. Liu, S. P. Ringer, J. M. Cairney, K. Wang, S. C. Smith and C. Zhao, *Nat. Commun.*, 2021, **12**, 1449.
- 126 Y. Wang, N. Gong, H. Liu, W. Ma, K. Hippalgaonkar, Z. Liu and Y. Huang, *Adv. Mater.*, 2023, **35**, 2302067.
- 127 L. He, M. Li, L. Qiu, S. Geng, Y. Liu, F. Tian, M. Luo, H. Liu, Y. Yu, W. Yang and S. Guo, *Nat. Commun.*, 2024, **15**, 2290.
- 128 R. Nartita, D. Ionita and I. Demetrescu, *Crystals*, 2024, **14**, 451.
- 129 Z. Li, C. Wang, Y. Liang, H. Jiang, S. Wu, Z. Li, W. Xu, S. Zhu and Z. Cui, *Appl. Catal., B*, 2024, **345**, 123677.
- 130 Z. Zhao, J. Sun, X. Li, S. Qin, C. Li, Z. Zhang, Z. Li and X. Meng, *Nat. Commun.*, 2024, **15**, 7475.
- 131 X. Liu, H. Lu, S. Zhu, Z. Cui, Z. Li, S. Wu, W. Xu, Y. Liang, G. Long and H. Jiang, *Angew. Chem., Int. Ed.*, 2023, **62**, e202300800.
- 132 J. Mai, Y. Zhang, H. He, Y. Luo, X. Zhou, K. Hu, G. Liu, M. K. Sugumar, C. T. John Low, X. Liu and R. Tan, *Mater. Today Chem.*, 2024, **38**, 102079.
- 133 W. Li, Z. Guo, J. Yang, Y. Li, X. Sun, H. He, S. Li and J. Zhang, *Electrochem. Energy Rev.*, 2022, **5**, 9.
- 134 H. Hu, Y. Zhao, Y. Zhang, J. Xi, J. Xiao and S. Cao, *Top. Curr. Chem.*, 2023, **381**, 24.
- 135 Y. Mu, T. Wang, J. Zhang, C. Meng, Y. Zhang and Z. Kou, *Electrochem. Energy Rev.*, 2022, **5**, 145–186.
- 136 Z. Pu, I. S. Amiin, R. Cheng, P. Wang, C. Zhang, S. Mu, W. Zhao, F. Su, G. Zhang, S. Liao and S. Sun, *Nano-Micro Lett.*, 2020, **12**, 21.
- 137 X. Wang, L. Zhao, X. Li, Y. Liu, Y. Wang, Q. Yao, J. Xie, Q. Xue, Z. Yan, X. Yuan and W. Xing, *Nat. Commun.*, 2022, **13**, 1596.
- 138 E. Chukwu and M. Yang, *Chem. Catal.*, 2023, **3**, 100735.
- 139 K. Jiang, B. Liu, M. Luo, S. Ning, M. Peng, Y. Zhao, Y.-R. Lu, T.-S. Chan, F. M. F. de Groot and Y. Tan, *Nat. Commun.*, 2019, **10**, 1743.
- 140 J. Chen, E. Kemly, M. Croft, Y. Jeon, X. Xu, S. A. Shaheen and P. H. Ansari, *Solid State Commun.*, 1993, **85**, 291–296.
- 141 K. L. Zhou, Z. Wang, C. B. Han, X. Ke, C. Wang, Y. Jin, Q. Zhang, J. Liu, H. Wang and H. Yan, *Nat. Commun.*, 2021, **12**, 3783.
- 142 Y. Zhu, M. Klingenhof, C. Gao, T. Koketsu, G. Weiser, Y. Pi, S. Liu, L. Sui, J. Hou, J. Li, H. Jiang, L. Xu, W.-H. Huang, C.-W. Pao, M. Yang, Z. Hu, P. Strasser and J. Ma, *Nat. Commun.*, 2024, **15**, 1447.
- 143 R. Subbaraman, D. Tripkovic, K.-C. Chang, D. Strmcnik, A. P. Paulikas, P. Hirunsit, M. Chan, J. Greeley, V. Stamenkovic and N. M. Markovic, *Nat. Mater.*, 2012, **11**, 550–557.
- 144 M. T. Greiner, T. E. Jones, S. Beeg, L. Zwiener, M. Scherzer, F. Girgsdies, S. Piccinin, M. Armbrüster, A. Knop-Gericke and R. Schlögl, *Nat. Chem.*, 2018, **10**, 1008–1015.
- 145 J. Park, J. H. Lim, J.-H. Kang, J. Lim, H. W. Jang, H. Shin and S. H. Park, *J. Energy Chem.*, 2024, **91**, 155–177.
- 146 S. Li, J. Yan, X. Chen, C. Ni, Y. Chen, M. Liu and H. Su, *Mater. Today Catal.*, 2024, **7**, 100068.
- 147 Y. Liang, J. H. K. Pfisterer, D. McLaughlin, C. Csoklich, L. Seidl, A. S. Bandarenka and O. Schneider, *Small Methods*, 2019, **3**, 1800387.

